8-2018

Micron/Nano Structure Creation Through Dual Pulse Femtosecond Laser Surface Processing

Nicholas Roth
University of Nebraska-Lincoln, nroth2@gmail.com

MICRON/NANO STRUCTURE CREATION THROUGH DUAL PULSE FEMTOSECOND LASER SURFACE PROCESSING

By

Nicholas Roth

A thesis

Presented to the Faculty of

The Graduate College at the University of Nebraska

In Partial Fulfillment of Requirements

For the Degree of Master of Science

Major: Electrical Engineering

Under the Supervision of Professor Dennis Alexander

Lincoln, Nebraska

July, 2018

MICRON/NANO STRUCTURE CREATION THROUGH DUAL PULSE FEMTOSECOND LASER SURFACE PROCESSING

Nicholas Roth, M.S.

University of Nebraska, 2018

Advisor: Dennis Alexander

A new technique has been developed for creating multiscale micro/nanoscale surfaces on metals. This technique is based on past work in femtosecond laser surface processing (FLSP) and dual pulse laser induced breakdown spectroscopy (LIBS). Using a femtosecond laser, pulse pairs were created with varying pulse separations between 0 ps to 500 ps. The creation of surface structures with dual pulse FLSP was studied on Ag, Cu, Ti, Al, Ni, and 304 stainless steel in relation to pulse separation.

Using dual pulse FLSP micro/nano structures have been created for the first time on silver. The silver structures are multiscale in nature with an average height of 32 μm and a nanoparticle aggregate covering them. This dual pulse method also reduces the needed fluence to create micro/nano structures on copper when compared to FLSP performed with a single pulse train. It was found that the formation of these surface structures is dependent on the pulse separation between pulse pairs. The initial pulse temporarily decreases the material reflectivity which causes increased absorption of the second pulse. The reduction in reflectivity increases the laser energy being coupled into the material.

Acknowledgements

There's no way to properly express how grateful I am to everyone that has helped me along the way. I could not make it to where I am today if I didn't have a support network of friends, family, students, and faculty helping me along the way. These people are some of the kindest, hardest working, and most talented I have ever meet.

I'd first like to express my thanks to all the faculty at the University of Nebraska. Especially my advisor Dr. Alexander who always pushed us to better ourselves. I was also grateful to have Dr. Zuhlke and Dr. Anderson available who were both amazingly knowledgeable about their fields of study. I'm also grateful for all the faculty that I interacted with over the course of my education.

While working within the center for electrooptic and functionalized materials I meet a great group of people. The other members of my lab group Chris, Kim, John, Nick, Alfred, Ryan, Arron, Conner, and Chongji all have amazing potential. I'll be interested to see what happens with all of you.

And finally, my friends and family have been amazing. I couldn't ask for a better group of friends who always seemed to be there for me. My family has been great and wonderfully supportive. I hope I've made them proud.

Table of Contents

List of figures

Chapter 1: Introduction

1.1 Femtosecond laser surface processing

Femtosecond laser surface processing (FLSP) is a developing technique used to modify the microscale and nanoscale surface topography of bulk materials using ultrashort pulse laser ablation [1], [2]. The surface created with FLSP is multiscale in dimensions, having both micron and nanoscale surface features. This multiscale surface has applications in heat transfer [3][4][5], medical technology [6], and self-cleaning surfaces [7]. FLSP can be used to change the surface chemistry [8], optical properties [9], and electrical properties [10] of a material.

The surface topography created through FLSP can be produced over larger surface areas by rastering single or multiple laser beams over the surface Laser rastering is the process of scanning a substrate with a laser having a Gaussian intensity distribution. The total integration of the energy for a given spot creates a homogeneous self-organized topography of micron and nanoscale features that is highly reproduceable.

With recent developments in laser technology, the minimum pulse length for lasers has reached the attosecond regime and laser manufactures are developing easy to use, stable femtosecond laser systems for use in industry. With ultrashort pulse laser technology gaining popularity in industry there is still much that is not understood about the physics behind ultrashort pulse laser interactions with matter. In addition, this thesis introduces dual-pulse concepts as another unique aspect of ultrashort pulse laser interaction with matter. This thesis attempts to provide a few theories to explain the differences between single-pulse and dual-pulse matter interactions.

1.2 Dual-pulse laser interaction with materials

Within the field of laser induced breakdown spectroscopy (LIBS) one recent area of study is double or dual laser pulse LIBS. In the context of this thesis dual-pulse (also sometimes referred to as double pulse) is reference to laser pulses which are separated by at most hundreds of picoseconds. Dual-pulse LIBS compared to single-pulse LIBS has been shown to improve the signal intensity [11], increase the amount of material removed [12], increase the electron density [13], influence the plasma temperature [14], and change the material ablation threshold [15]. Although dual-pulse LIBS provides some guidance for dual-pulse laser matter interactions. There appears to be little published related to laser machining, especially raster scanning with a dual-pulse setup. In general, LIBS is performed at high fluences with a small laser spot. In this thesis, we explore a wide range of laser fluences and pulse counts on metallic surfaces. Special focus is given to noble metals where it is difficult to obtain self-organized surface features with a single-pulse FLSP.

1.3 Noble metals

Noble metals are generally classified as Au, Ag, and the platinum group which consists of Pt, Pd, Rh, Ir, Ru, and Os.[16] In some cases, Cu (due to its high thermal conductivity and electron dynamics) is included in this group of special metals. The main characteristics of noble metals is their resilience to corrosion and their catalytic potential. Much like the noble gases, noble metals are less likely to react with other elements. The group 11 elements are sometimes referred as the coinage metals and are considered a subset of noble metals and include Cu, Ag, and Au. These elements have unique properties because of their high electrical and thermal

conductivity. These three metals have higher conductivity values than any element on the periodic chart.

The noble metals have many applications in industry because of their antimicrobial properties, use as efficient thermal/electrical conductors, and corrosion resistance properties. The antibacterial properties of Ag have been known for many years, and recently Ag nanoparticles have become useful alternatives to antibiotics. Likewise, copper is used throughout the electronics industry as a relatively inexpensive conductor.

Chapter 2: Literature Review

2.1 Micro/nanostructure creation through FLSP

FLSP creates a multiscale surface topography on a material without changing its bulk properties. The surface will have microscale features such as mounds, pyramids, spikes, or columns with randomized nanoscale features consisting of nanoparticles [1]. The type of surface structures created is greatly dependent upon the beam profile, the number of laser pulses, and the peak fluence.

The beam profile and spot size on a sample surface for a laser focused through a plano-convex lens is determined by beam alignment and the distance between the sample and the lens. As the sample is moved towards focus the spot size decreases and power density increases. LIBS work by Zuhlke provides great detail on the focusing dynamics on either side of focus[17]. For laser processing using a Gaussian profile an important laser parameter to track is the peak fluence, which is given in **Error! Reference source not found.**.

$$F = \left(\frac{2\,E_p}{\pi \omega_0^2} \right), \qquad (1)$$

Where E_p is the pulse energy and ω_0 is the $1/e^2$ gaussian beam radius at the sample surface. This measurement is generally given in $\left[\frac{J}{cm^2}\right]$.

Zuhlke et al. suggested that structures created through FLSP using different processing parameters can be organized into several unique types of surface structures.[18] For nickel Zuhlke et al. described two types of surface structures in detail, above surface growth (ASG) mounds, and below surface growth (BSG) mounds [1]. ASG mounds have peaks that develop above the original sample surface while BSG mounds have peaks below the original substrate surface. Structure creation is initially dominated by fluid flow dynamics where precursor sites become conical structures. The geometry of these surface structures scatters and reflects light leading to reduced ablation of precursors strucutres and increased ablation of areas around precursors. This geometric process of valley formation is called preferential valley ablation (PVA) developed by Zuhlke et al. explaining the development of valleys during FLSP.[1] Fig. 2.1 demonstrates the different stages of BSG structure formation beginning with precursor sites and then the development of structures through PVA.

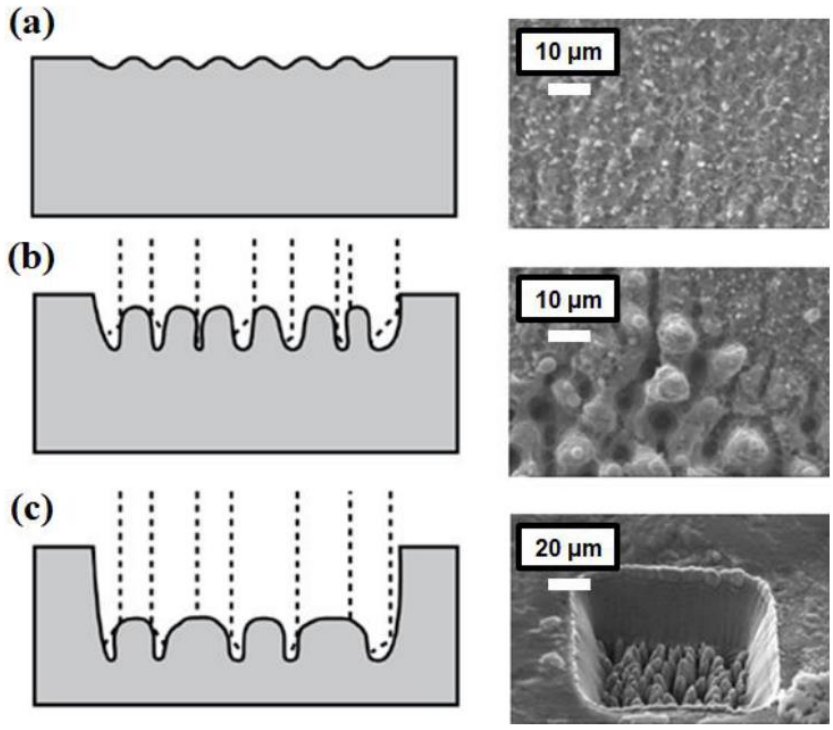

Figure 2.1: BSG mound creation progression through different stages adopted from [19] **a) precursor site formation b) the beginning of structure formation by PVA c) developed micro/nano surface structures.**

BSG mound structure formation is dominated by PVA and BSG mounds are created at lower fluences compared to ASG mounds. ASG mounds develop into structures through a mixture of PVA, fluid mechanics, and material redeposition. The surface topography of ASG mounds is dominated by pits and pillars created through vapor redeposition and fluid flow.

Creating uniform micron/nanoscale surface structures over larger area on bulk materials requires rastering the laser over the material surface. This is done by translating the sample through a stationary laser beam. Assuming the optical system is correctly aligned, the laser spot observed on the sample will have a Gaussian distribution. The number of pulses incident on any one location on the sample can be found through equation 2.

$$N = 2.68\frac{\omega_0^2 f}{v\, d}, \quad (2)$$

In equation 2 v is the scan velocity, d is the distance between raster scans, and f is the laser repetition rate. Figure 2.2 is a graphic of a laser rastering scanning pattern where d is the rastering pitch with a total rastered area of $A = xy$. The value of N is dimensionless and represents the number of times a single point on the sample surface will be irradiated by a laser pulse of radius ω_0.

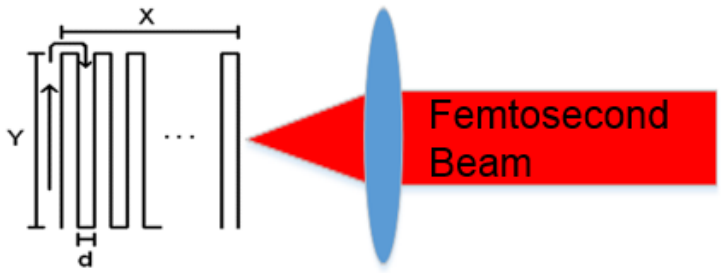

Figure 2.2: Diagram of laser rastering.

The range of surface topographies that can be created using FLSP has been studied extensively on nickel by Zuhlke et al. [18]. SEM images of a range of structures created by applying FLSP to nickel are included in Fig. 2.3, which is organized to generally following the trend of increasing fluence along the x axis and increasing pulse count along the y axis. These unique structures were all created through a modification of either the peak fluence or a change in the pulse count. With a wide range of surface topographies, FLSP is a useful tool for material modification.

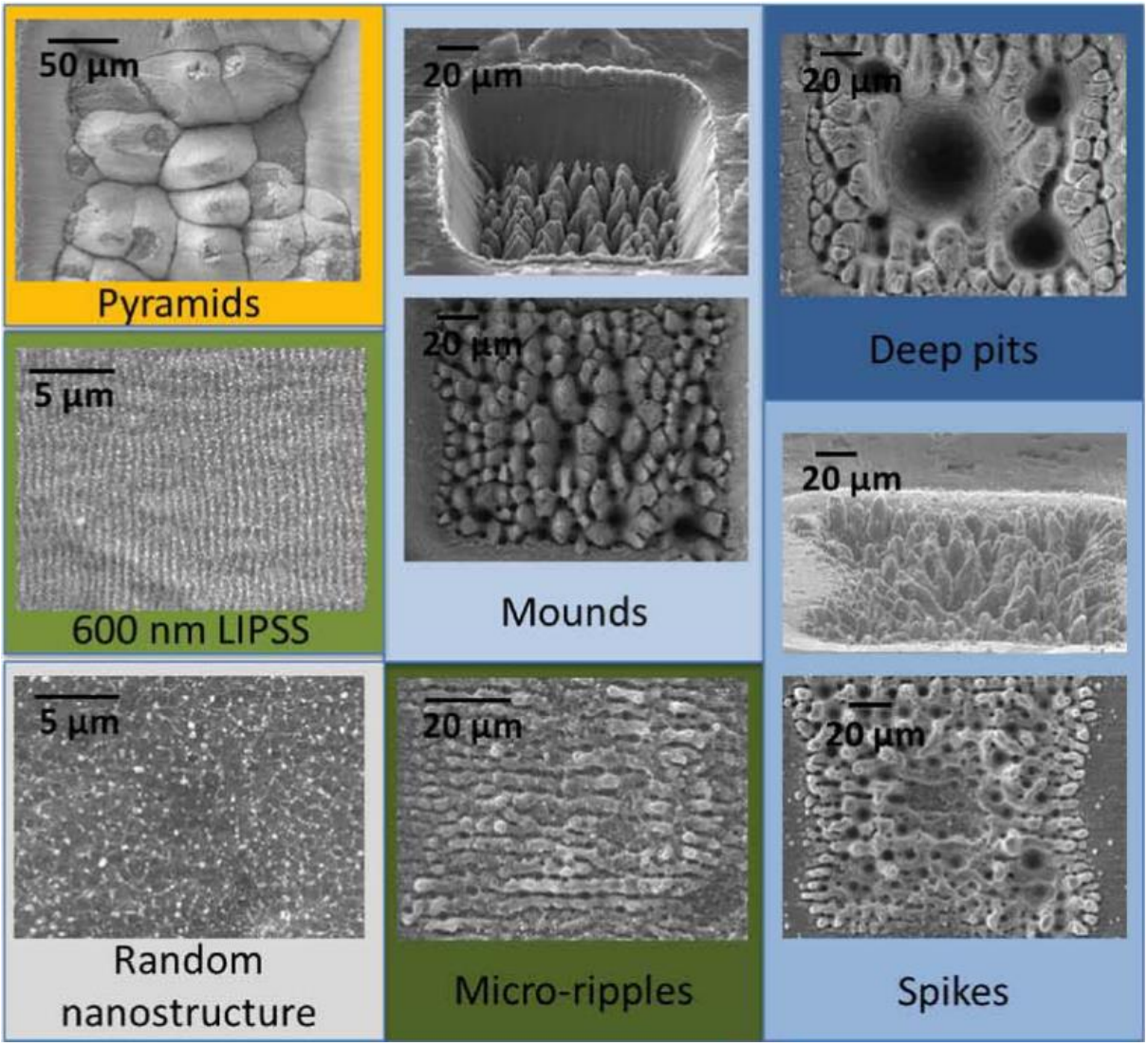

Figure 2.3: The range of surface structures created through FLSP in nickel adopted from [18]**.**

2.2 Drude model and plasma frequency

The Drude model is a special case for the Lorenz model for a harmonic oscillator. The Lorenz model is used to explain the dynamics of an electron with multiple forces acting on it. Within a conductor an electron can be treated as a free particle and the crystal lattice can be

ignored. This creates a linear relationship between current density and the electric field without dampening effects [20].

Light is modeled as an AC field at the material interface acting as an external force on the electrons. Depending on the wavelength of light (the AC field frequency), a field propagating towards a wall of electrons will either reflect or be absorbed into the material. The plasma frequency, given in **Error! Reference source not found.**, is lowest frequency an electric field can be oscillating to be absorbed by a material.

$$\omega_p = \left(\frac{e^2 N_f}{\varepsilon m^*}\right)^{\frac{1}{2}}, \quad (3)$$

2.3 Ultrashort pulse laser interaction with matter

Short pulse laser technology is a new field of research that was aided with the development of chirped pulse amplification (CPA), which was first applied to lasers in the 1980s [21]. Laser pulse durations in the <50 femtosecond range and pulse energies in the >1 mJ range are common in the current generation of femtosecond lasers. These short pulse durations cause high peak power (P_p) given by the following equation:

$$P_p = 0.88\frac{E_p}{\tau}, \quad (4)$$

Where E_p is the pulse energy, and τ is the pulse duration. Femtosecond lasers usually have a Gaussian temporal distribution of the laser energy, so in Eq. 4 the 0.88 conversation factor is used to convert between a square pulse and a Gaussian pulse. A typical femtosecond laser will have peak powers in the gigawatt range. Compared to a continuous laser a femtosecond pulse laser will have a low average power while having a much higher peak power.

There are many advantages to having extremely short and high peak power pulses. Using femtosecond pulses, measuring such things as plasma physics, chemistry events, and other phenomenon, which occur over short time scales has been demonstrated. Potter et al. demonstrated a method for measuring a chemical reaction with a femtosecond laser [22]. The extremely short pulses also decrease the rate at which material is damaged by the heat effected zone (HAZE), which is very important in processing of metal surfaces. Longer pulse lasers can change the bulk properties of a material by damaging it and causing microcracks.

2.4 Dual-pulse laser interaction

Within the field of laser induced breakdown spectroscopy (LIBS), one recent area of study is the use of double or dual laser pulses. Dual-pulse LIBS compared to single-pulse LIBS has been shown to improve the signal intensity [11], increase the amount of material removed [12], increase the electron density [13], influence the plasma temperature [14], and change the ablation threshold [15]. In the context of this thesis dual-pulse or double-pulses is reference to laser pulses which are separated by at most hundreds of picoseconds.

LIBS is used to study the elemental makeup of a material by measuring the spectrum of the laser induced plasma. The dual-pulse research completed in this thesis will be focused on material changes rather than any signal measured by a spectrometer.

Chapter 3: Experimental Setup and Analysis

3.1 Dual-pulse experimental setup

The dual-pulse experimental setup is divided into 3 parts. The femtosecond laser, delay stages with a beam splitter and beam combiner, and the machining setup. The purpose of this

section is to describe in detail the three parts that makeup a dual-pulse setup used in this work for creating FLSP surfaces.

The first part of the experimental setup is the Astrella femtosecond laser system produced by Coherent. Outside the Astrella femtosecond laser there is a half-waveplate and polarizer combination used for power attenuation into the dual-pulse setup. A fused silica thin film polarizer from Eksma optics was used for the power attenuator. According to the manufacturer website the polarizer reflects 99.5% of s-polarized light and transmits 95.0% of p-polarized light.

The linearity of polarization entering the dual-pulse setup was important for alignment due to the differing beam paths and differing optical components. The beam path to the dual-pulse experimental setup followed the reflected beam (s-polarization) from the attenuation polarizer because the linearity of polarization was greater than the transmitted beam.

The Astrella femtosecond laser produces a 1 kHz pulse train of pulses with a pulse duration of 35 fs at a wavelength of 800 nm. The Astrella has a maximum pulse energy of 6 mJ which is reached by CPA. This system is self-contained and no modifications were made to it.

The pulse splitter, delay arm, and beam combiner make up the second part of the experimental setup and are shown in Figure 3.1. The laser pulse passes through an initial half-waveplate and polarizer which splits the pulse from the Astrella laser based on polarization. The s-polarized pulse (E-field oscillating perpendicular to the optical table) is directed to the mechanical delay stage and the p-polarized pulse (E-field oscillating parallel to the optical table) is directed to the air-bearing, computer controlled delay stage. The length of each delay arm (the orange and yellow lines in Figure 3.1) are made approximately equal by adjustment of the mechanical stage.

The pulses arrive at the final polarizer and are overlapped spatially with a temporal delay determined by the position of the air-bearing stage. The air-bearing stage was used to control the delay between pulses while an autocorrelator was used to find the exact delay stage position at which the pulses were overlapped in time.

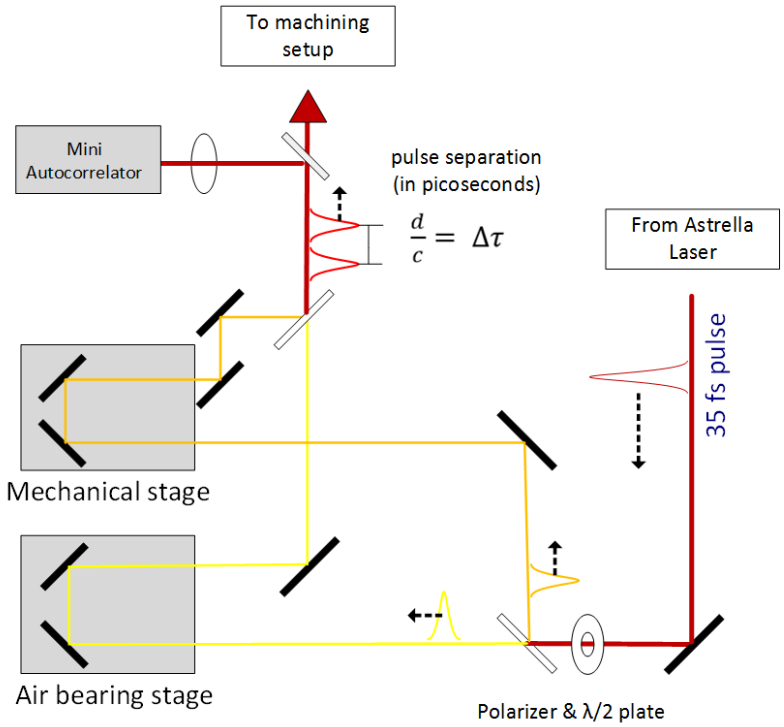

Figure 3.1: Pulse splitting, delay creation and beam combining portion of the experimental setup. The orange line is the path for the leading pulses and the yellow is the path of the delayed pulses. Red lines represent areas where both leading and delayed pulses are overlapped spatially. The final mirror reflecting light into the autocorrelator is removed after the delay between pulses has been measured.

The autocorrelator signal from a single-pulse train (one arm of the dual-pulse setup blocked) is shown in Figure 3.2(a). When a pulse train of double pulses are input into an autocorrelator the delayed pulse appears as two pulses symmetrically spaced on either side of the leading pulse as shown in Figure 3.2(b). The air-bearing stage is translated until both pulses arrive at the autocorrelator at the same time and the autocorrelator reads noise as shown in Figure 3.2(c). Once the stage position for zero delay was determined, the delay between the leading

pulse and the trailing pulse was set by the displacement of the air-bearing stage, which is accurate to 24 femtoseconds.

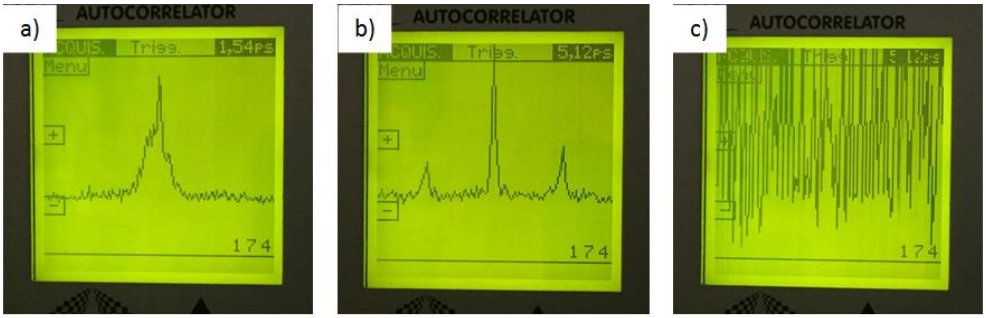

Figure 3.2: Mini-autocorrelator trace a) measuring only the initial pulse b) measuring pulse pairs arriving approximately within 500 fs of each other c) measuring pulse pairs arriving approximately at the same time.

The pulses are then directed to the machining stage which is shown in Figure 3.3. The laser was focused onto a sample with a fused silica plano-convex lens with a focal length of either 150 mm or 500 mm, depending on the experiment. The sample was placed on a Zaber computer controlled XY translation stage system with a Thorlabs computer controlled labjack for Z-positioning, which were used for sample positioning and rastering. An imaging system consisting of a CCD camera and a video monitor was used for sample positioning. Throughout this thesis changes will be made to the experimental setup depending on the experiment. When this occurs the author will note how the experimental setup was modified.

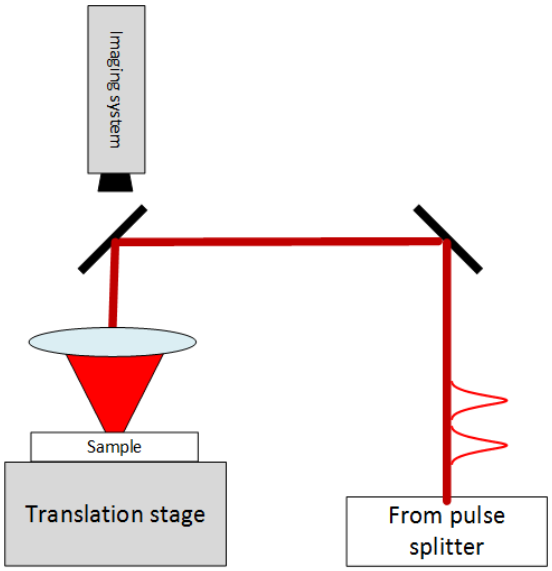

Figure 3.3: Dual-pulse FSLP machining stage.

A method of beam diagnostics used to ensure both pulses were overlapped spatially and traveling co-linearly onto the sample was the use of a Thorlabs CCD beam profiler. The profiler was placed on the Thorlabs labjack Z-translation stage and moved through its full height range. Figure 3.4 is an image of the beam profile for the initial beam only in Fig. 3.4(a) and then adding the delayed beam in Fig. 3.4(b) without moving the profiler.

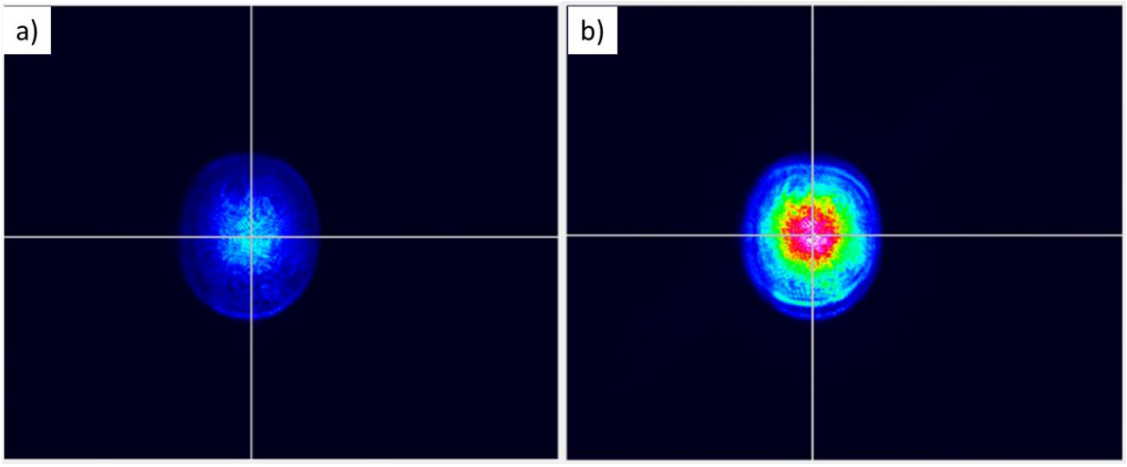

Figure 3.4: Beam profile of a) the initial pulse with the delayed pulse blocked b) both pulses overlapped.

3.2 Surface analysis equipment

To better understand the physics behind dual-pulse FLSP, this thesis will cover several experiments that were performed. This section of the thesis describes the surface analysis equipment used. Equipment and facilities were within the Center for Electro-Optics and Functionalized Surfaces and the Nano-Engineering Research Core Facility at UNL.

3.2.1 Philips XL30 Environmental Scanning Electron Microscope

The bulk of the SEM images were taken with the Philips XL30 Environmental Scanning Electron Microscope with a resolution of 25 nm. An SEM was preferred over an optical microscope. The structures created through FLSP are on the micron to nanometer scale and the resolution of an optical microscope would be insufficient to fully characterize the surface. The surface topography is highly variable in the micron range. An SEM is able to resolve the entire micro/nanoscale topography of the samples created [23].

3.2.2 Helios NanoLab 660 with focused ion beam etching

The surface structures created with FLSP can be in the nanometer scale with nanoparticles, nano-hairs, and other nanoscale structures. To resolve these nanoscale structures the Helios NanoLab 660 was used to take high resolution SEM images. This SEM has a max resolution of 0.8 nm at an electron potential of 30 kV [24].

The Helios 660 also has ion beam etching capability, which was used to make cross-sections of the structures created with dual-pulse FLSP. The mound is first sputtered with platinum to create a protective surface, then gallium ions impact the mound and remove material down to a 4 nm

resolution. Structure cross-sectioning was a useful tool for analyzing the dynamics of the surface structure creation. These cross-sections provide insight into the fluid dynamics of dual-pulse FLSP, which were first observed for single-pulse FLSP by Zuhlke et al. [7].

3.2.3 Keyence VK-X200

The Keyence VK-X200 microscope is a laser scanning confocal microscope (LSCM) and was used for creation of 3D maps of the sample surface and making quantitative measurements of surface structure characteristics. The primary values determined with this instrument were average structure height and surface roughness. This instrument was also a useful tool for building a 3D map of the surface structures created using dual-pulse FLSP and has statistical analysis capabilities not available with the SEM.

The LSCM works through scanning the sample surface with a 408 nm laser probe beam and using the reflected light to build a 3D mapping of the surface. Only light that is at the focal point of the laser can be reflected back onto the photo receptor. This occurs because the reflected light must pass through a pinhole to reach the photodetector, which blocks out light that is outside of focus. The Keyence creates a 2-D rastered image of the surface at each height step with minimum height step size of 0.5 nm. Those 2D images are stacked on top of each other creating a 3D image of the sample surface.

Chapter 4: Results

4.1 Dual-pulse laser ablation versus single-pulse laser ablation

Distinct differences between single-pulse laser ablation and dual-pulse laser ablation are shown in Fig. 4.1. Figure 4.1(a) was created with a train of 2,500 single pulses at a pulse energy of 3.0 μJ. Figure 4.1(b) was created with a train of 2500 pulse pairs with pulse energies of 1.5 μJ per pulse. The surface structures within the dual-pulse ablation crater were similar to the structures found in Zuhlke's work which features deep pits and surface mounds [1]. Even for fluences greater than 10 J/cm^2 surface structures never formed using single-pulse laser ablation.

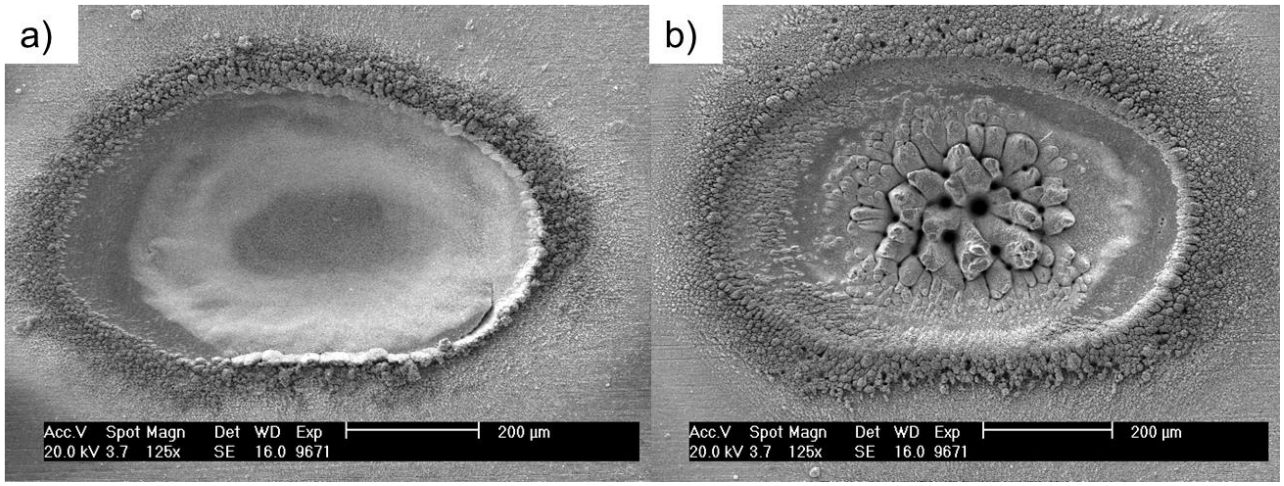

Figure 4.1: Ablation craters in silver created with a) 2,500 single pulses at 3.0 μJ per pulse b) 2,500 pulse pairs at 1.5 μJ per pulse.

4.2 Dual-pulse structures created through stationary ablation

Initial dual-pulse FLSP experiments included producing stationary ablation craters on multiple materials. A progression of selected ablation craters on silver (99.99 % pure), copper (101), aluminum (1100), stainless steel (304), titanium (grade 2), and nickel (200) are shown in Fig. 4.2. The SEM images in Figure 4.2 were selected from an experiment completed at pulse separation intervals of 5 ps from 0 ps to 110 ps. Each ablation spot was created with 3,000 pulse pairs with differing pulse separation, which is given at the top of the figure. The leading pulses (orange path in Figure 3.1) and delayed pulses (yellow path in Figure 3.1) had different beam characteristics because of the differing optical elements along their respective beam paths. The characteristics of each beam are included in Table 1.

Table 1: Beam Characteristics

	Pulse energy	Beam diameter	Peak fluence	Pulse width	Peak power
Initial pulse	2.3 mJ	610 µm	1.55 J/cm^2	75 fs	27.0 GW
Delayed pulse	2.3 mJ	520 µm	2.17 J/cm^2	55 fs	36.8 GW

By inspection of the SEM images in Figure 4.2 it is evident that an increase in pulse delay promoted structure growth in silver and copper while inhibiting structure growth in aluminum, titanium, stainless steel, and nickel. Figure 4.3 includes larger SEM images of select dual-pulse ablation craters from Figure 4.2. The SEM images on the top are at zero pulse separation and a pulse separations where fully developed surface structure are created in silver and copper. The SEM images at the bottom of Figure 4.3 are at zero pulse separation and a pulse separation where structures no longer form on stainless steel and titanium. Structure formation

occurs at a delay of 20 ps for copper while silver requires a delay around 110 ps. In stainless steel and titanium structure formation stops at pulse separations of 80 ps and 110 ps respectively.

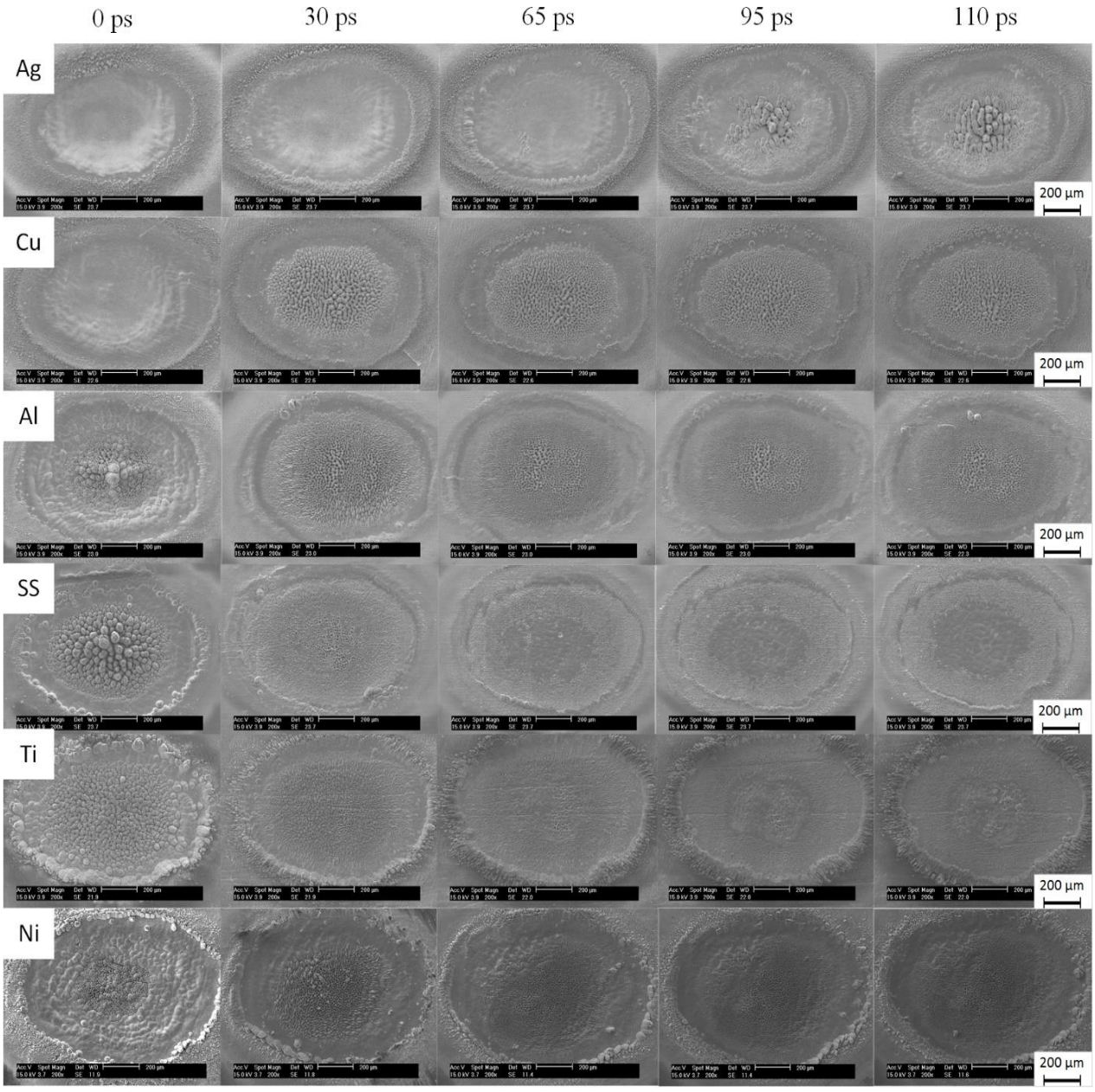

Figure 4.2: Stationay ablation spots created through dual pulse laser ablation on different materials and at different pulse delays given on top. Each ablation spot was created with 3,000 pulse pairs with the initial pulse having a peak fluence of 1.55 J/cm^2 and the delayed pulse a peak fluence of 2.17 J/cm^2.

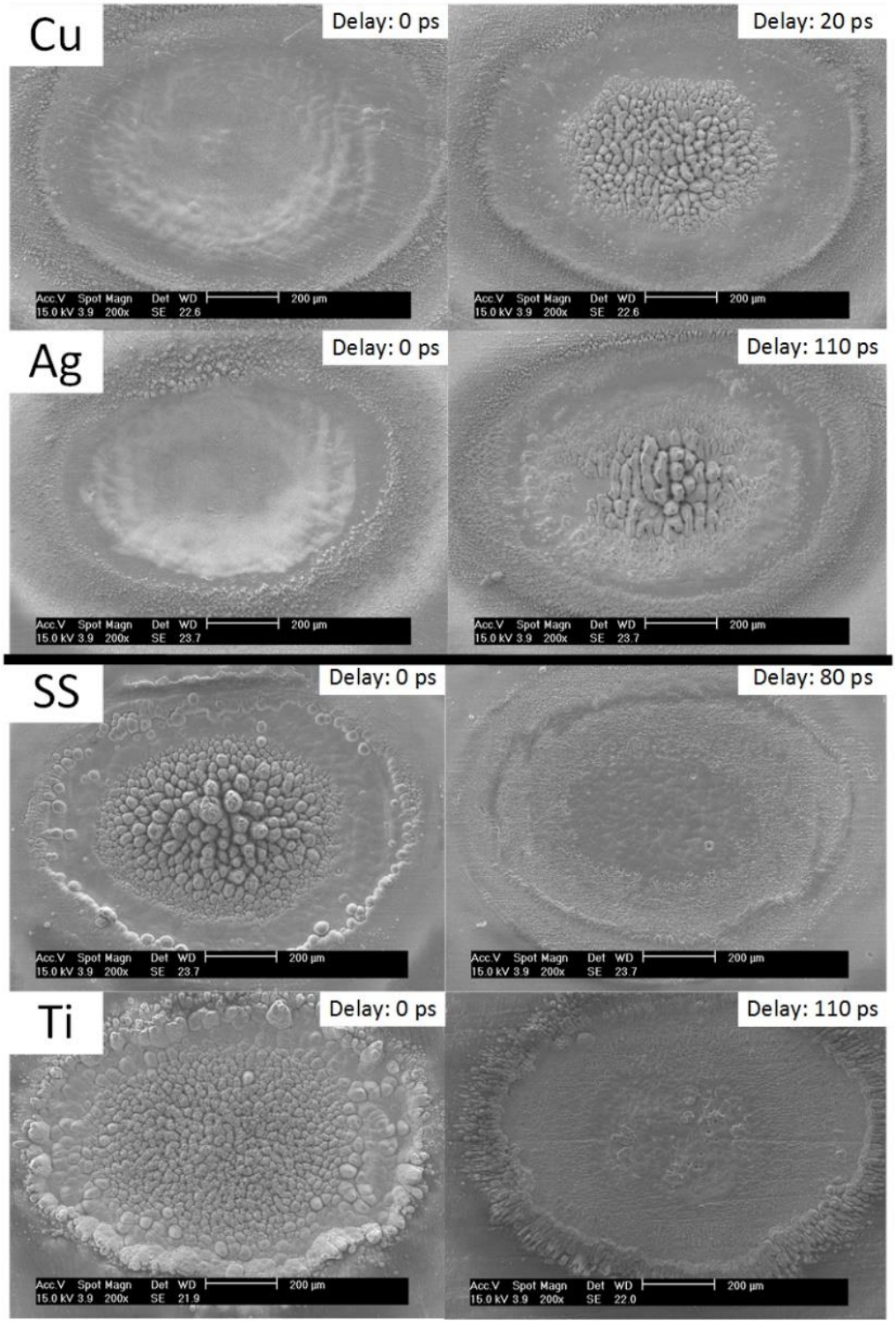

Figure 4.3: SEM images of ablation craters lowest pulse separation lengths that (top) create developed surface structures (bottom) fail to create surface structures.

For silver, if the pulse separation is increased past 300 ps the surface structures begin to disappear in the ablation craters at the same fluence and pulse count crated with increasing pulse separations are shown in Fig. 4.4. The energy from the initial pulse begins to thermally vaporize the substrate at around 300 ps. [25] The vapor cloud created by the initial pulse maybe inhibiting structure growth.

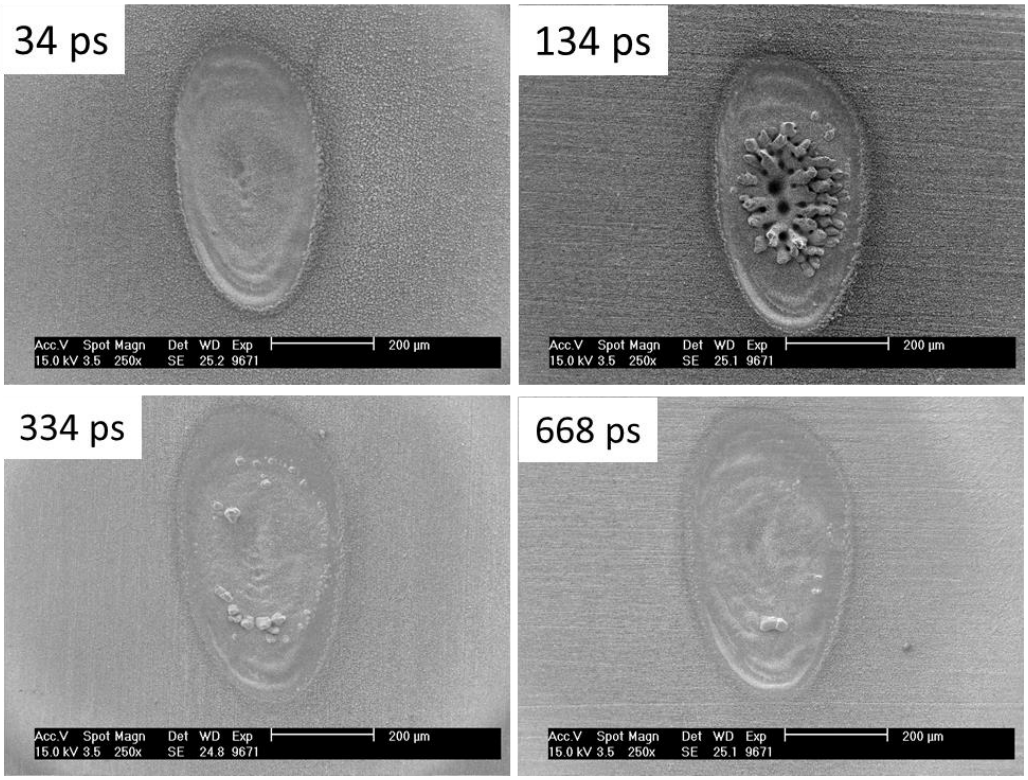

Figure 4.4: Dual pulse ablation craters in silver created with 500 pulse pairs with pulse energies of 1.5 µJ at differing pulse separations. Structures are not present in ablation craters with pulse separations past 300 ps.

Displayed in Fig. 4.5 is a progression of ablation craters on 304 stainless steel with increasing laser fluences. Each crater was created with 1,500 pulse pairs, and a pulse separation of 155 ps. At the lowest 2 fluences (Figure 4.5 top) pyramid structures begin to appear. As the fluence is increased (Figure 4.5 bottom row) micro ripples begin to form. [18] To fully

understand dual pulse ablation in stainless steel, a wider range of pulse counts and laser fluences would need to be studied.

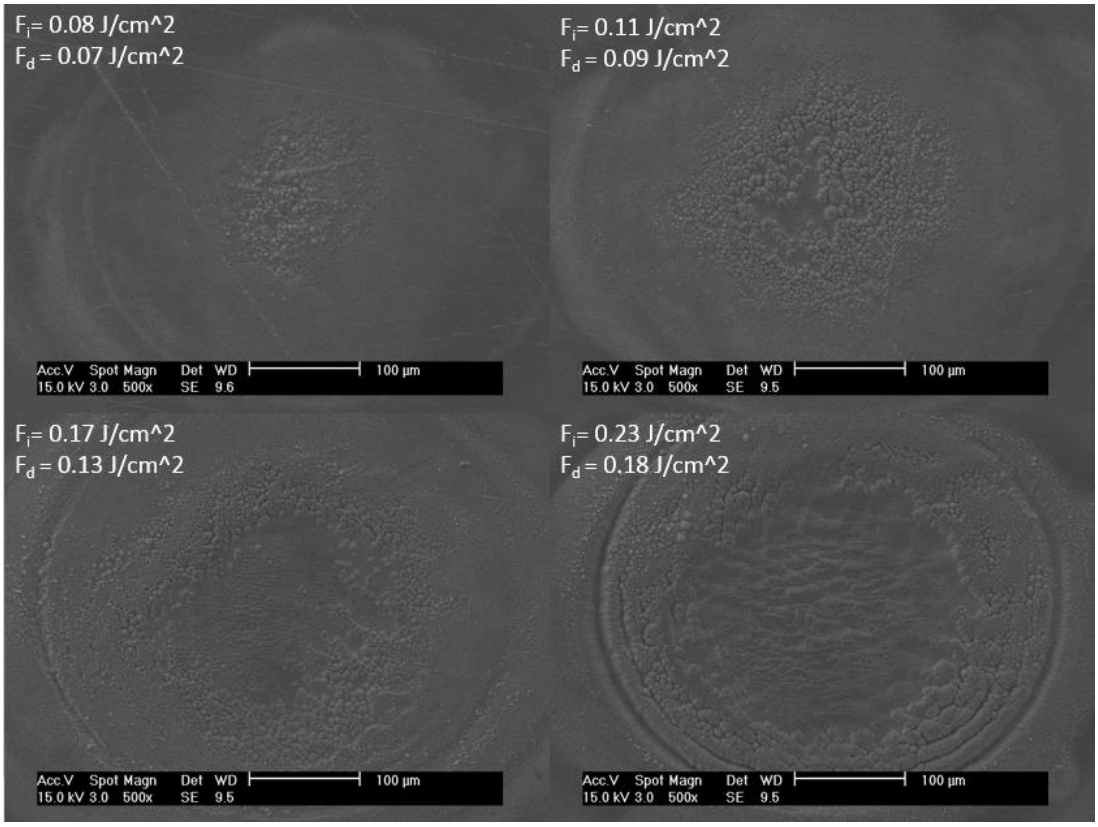

Figure 4.5: Dual pulse laser ablation craters on 304 stainless steel with a pulse delay of 155 ps. The fluence of the initial pulse and delayed pulse is shown as F_i and F_d respectively.

Dual-pulse laser ablation was also tested on gold using the same parameters given in Table 4.1, however, these samples were approximately 1 mm in thickness. Nanostructures have been created on gold in the past using femtosecond laser pulses [26]. Ablation craters in gold at the same parameters listed in Table 4.1 with pulse separations of 0 ps for Figure 4.6(a) and 110 ps for Figure 4.6(b),(c) and (d) are shown in Fig. 4.6.

A more gradual ablation method was attempted. The ablation crater in Figure 4.6(c) was produced using reduced peak fluences of 0.275 and 0.402 J/cm^2 for the initial pulse and delayed pulses respectively. The number of pulse pairs was increased from 3,000 to 10,000. This trend continues in Figure 4.6(d) with a peak fluence of 0.215 and 0.263 J/cm^2 for the initial and delayed pulse and a pulse pair count of 15,000.

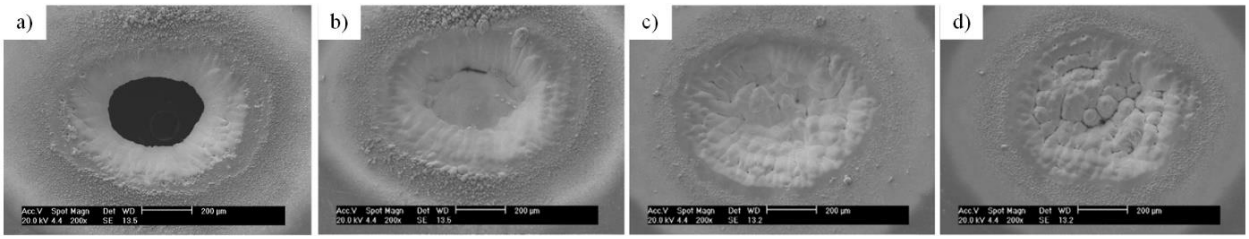

Figure 4.6: Ablation craters created in gold with a) the same beam properties given in table 4.1 and a pulse separation of 0 ps b) the same beam properties in table 4.1 with a pulse separation of 110 ps c) 10,000 pulse pairs at a peak initial/delayed pulse fluence of 0.275 and 0.402 J/cm^2 d) -15,000 pulse pairs at a peak initial/delayed pulse fluence of 0.215 and 0.263 J/cm^2.

The ablation crater in Figure 4.6(a) was deep enough to penetrate the gold sample when compared to Figure 4.6(b). Overlapped pulse pairs removed more material and created deeper craters when compared to pulse pairs with a separation of 110 ps. Reducing fluence and increasing pulse count began to develop large pyramid like structures like those reported by Zuhlke et al.[1]

The increased ablation depth with temporally overlapped pulses is not exclusive to gold. This phenomenon occurred in all materials used in this research. Increased ablation depth at pulse separations times of under 10 ps is consistent with past work on copper [18], aluminum [18], steel [7], and crystalline silicon [19]. Semerock et al. studied dual-pulse laser ablation in

copper, and aluminum.[27] The author found a reduction in ablation efficiency in copper and aluminum when the pulse separation time exceeded 1 ps. If the pulse separation time was extended past 10 ps, the dual pulse method removed less material when compared to a single pulse of equal energy. A graphic reproduced from Semerock et al. is shown in Figure 4.7 and displays the crater ablation depth when comparing single pulse ablation craters and dual pulse ablation craters.

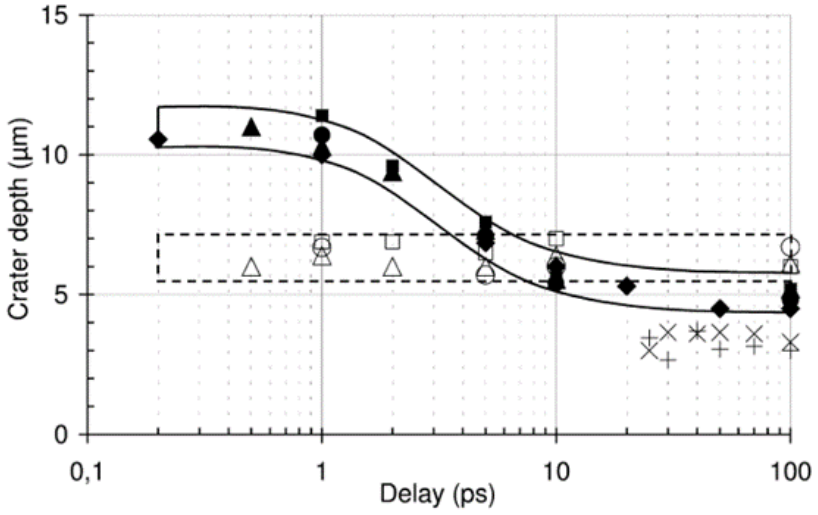

Figure 4.7: Dual-pulse ablation crater depth in copper in relation to increasing pulse pair delays. Adopted from [27]**. Filled in symbols represent dual pulse laser ablation.**

In past FLSP work the reproducibility of surface structures using the same fluence and pulse count has been noted. If dual-pulse FLSP was simply increasing the efficiency of material removal then we would expect a train of overlapped pulse pairs to create the similar structures as a train of single pulses.

4.3 High resolution surface and subsurface structure analysis

A cross section of dual-pulse FLSP surface structures were investigated to better understand how they form and to observe their subsurface structure. Figure 4.8 is an ablation crater created with a pulse delay of 128 ps, 1,500 pulse pairs, at a peak fluence for the initial pulses of 1.82 J/cm^2 and a peak fluence for the delayed pulses of 2.45 J/cm^2. This ablation spot was made on silver and was imaged with the Helios SEM.

From the angled SEM image in Figure 4.8(b) it can be seen that these structures are ASG mounds as the structures have peaks that reach above the original substrate. These structures resemble the spike-like surface structures created in nickel and shown in Figure 2.3. The rounded off bulb-like features in Figure 4.8(c)(d) are like those found in spikes. Those structures are known to be formed through PVA, material redeposition, and fluid mechanics, which is illustrated in Figure 4.9 [1]. A feature of ASG mounds are deep pits created by surface geometry of laser pulses reflecting off of existing mounds. These pits can be found next to the mound that is circled in Figure 4.8(a).

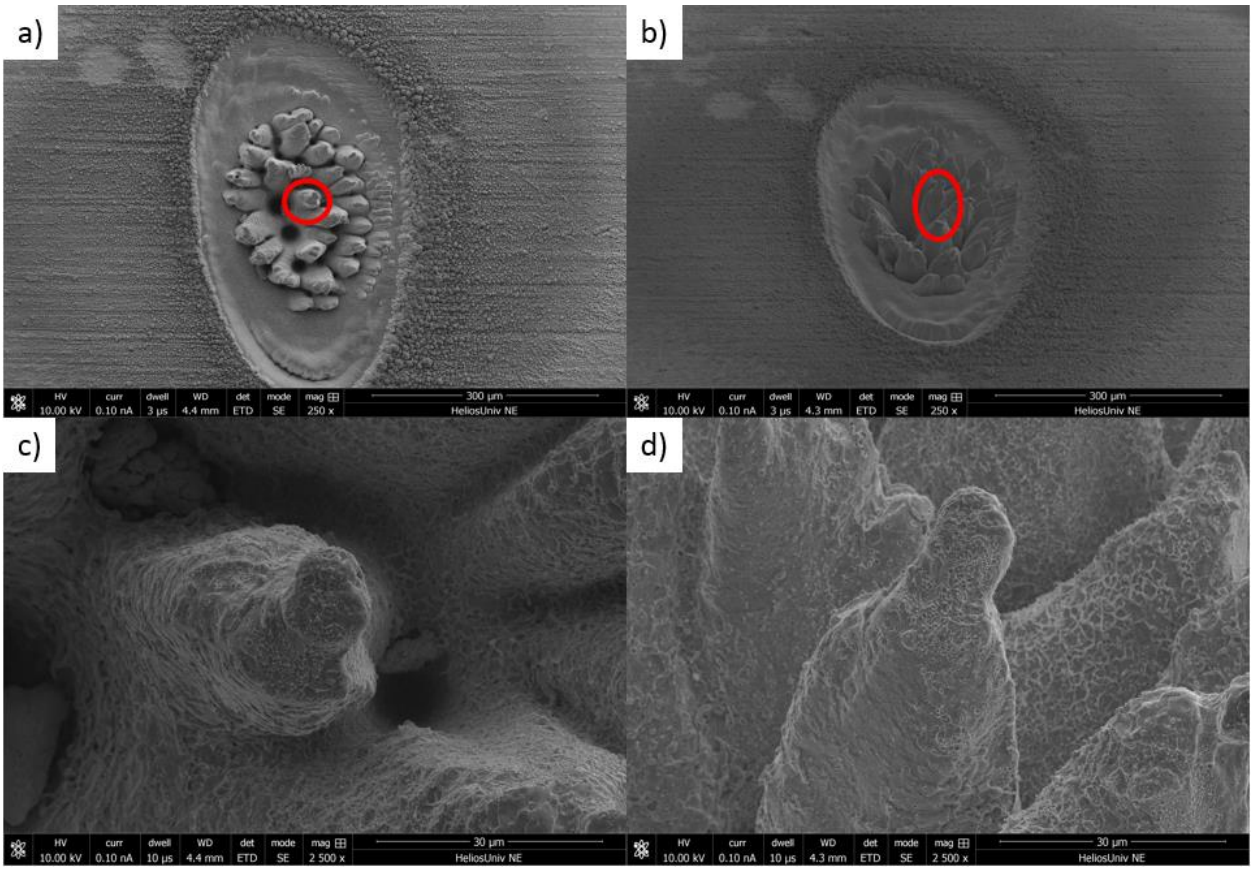

Figure 4.8: Dual pulse ablation crater in silver imaged with the Helios high resolution a) top down view b) mounds viewed at 45 degrees c) higher magnification image of circled mound in (a) d) higher magnification image of circled mound in (b).

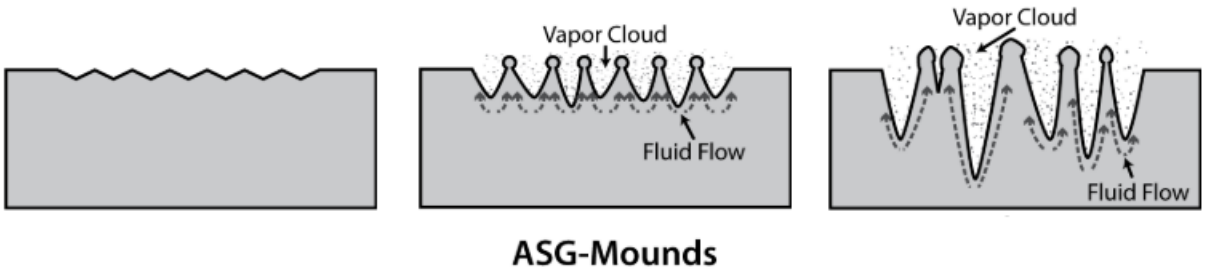

Figure 4.9: ASG mound growth through PVA, redeposition, and fluid flow. Adopted from [1]**.**

Signs of material redeposition or fluid flow are more evident in Figure 4.10, which includes high-resolution SEM images of the circled surface structure from Figure 4.8. At this magnification we can view the nanostructure of these materials and the multiscale nature of the surface topography becomes clear. These spike structures are in the range of 80 μm in height. Nanoparticles cover the surface some of which are in the 100s of nanometers while others are in the 10s of nanometer range.

The fluid-like nature of material redeposition is also noticeable. Nanostructures that resemble webbing or strands with fluid-like bubbles are shown in Figure 4.10(b). These web-like nanostructures have been created on silver in the past through femtosecond laser ablation [28]. Figure 4.11 is an SEM image taken from Dai et. al. published in 2012. These structures were created on a 200 nm silver film covering a glass substrate with a pulse count of 5 at a fluence of 1.57 J/cm^2. The author believed these microstructures formed through nanomelting and a phase explosion caused by a rapid rise in temperature.

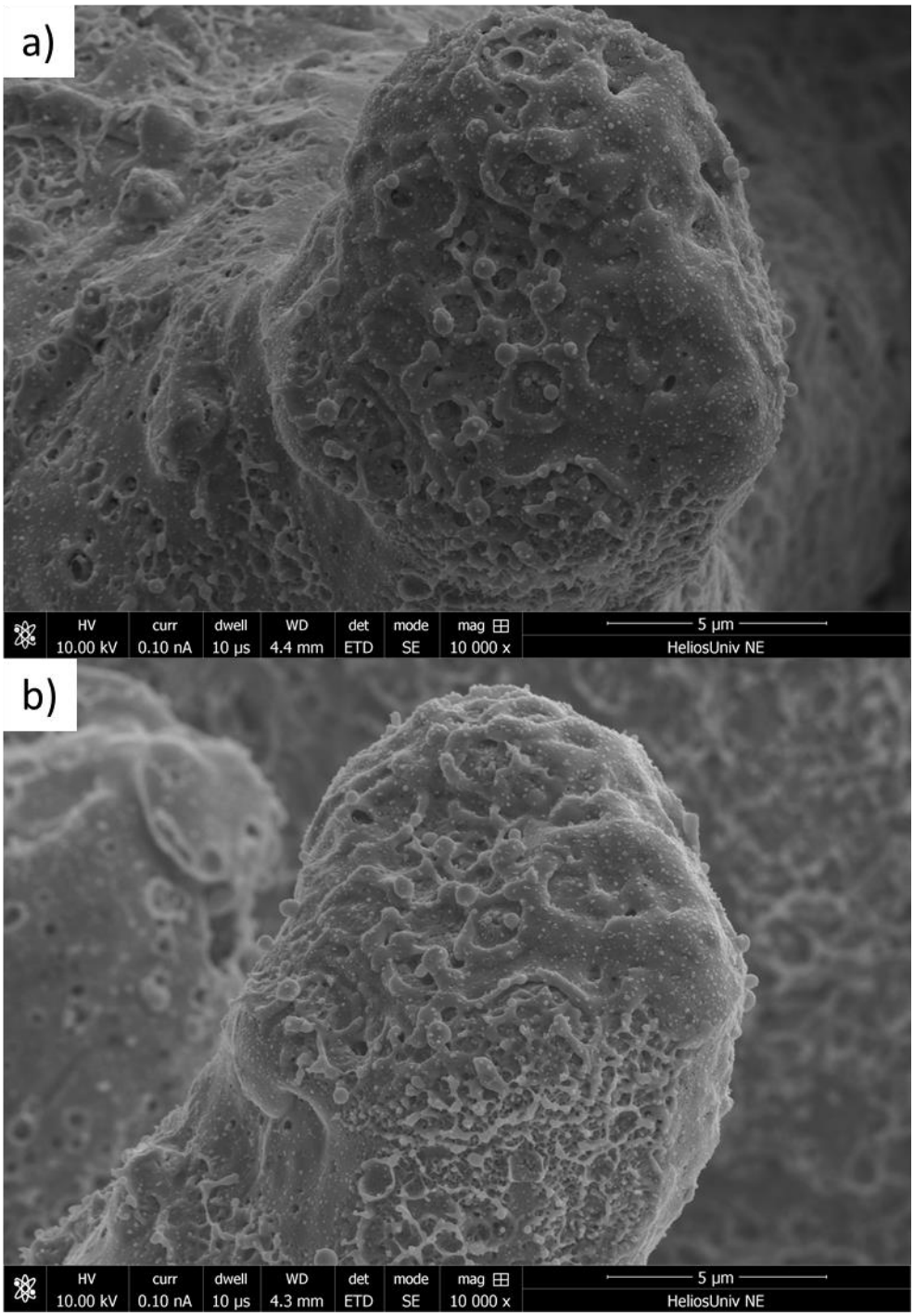

Figure 4.10: High resolution SEM images of the structures found in a) Fig. 4.7(c) b) Fig. 4.7(d).

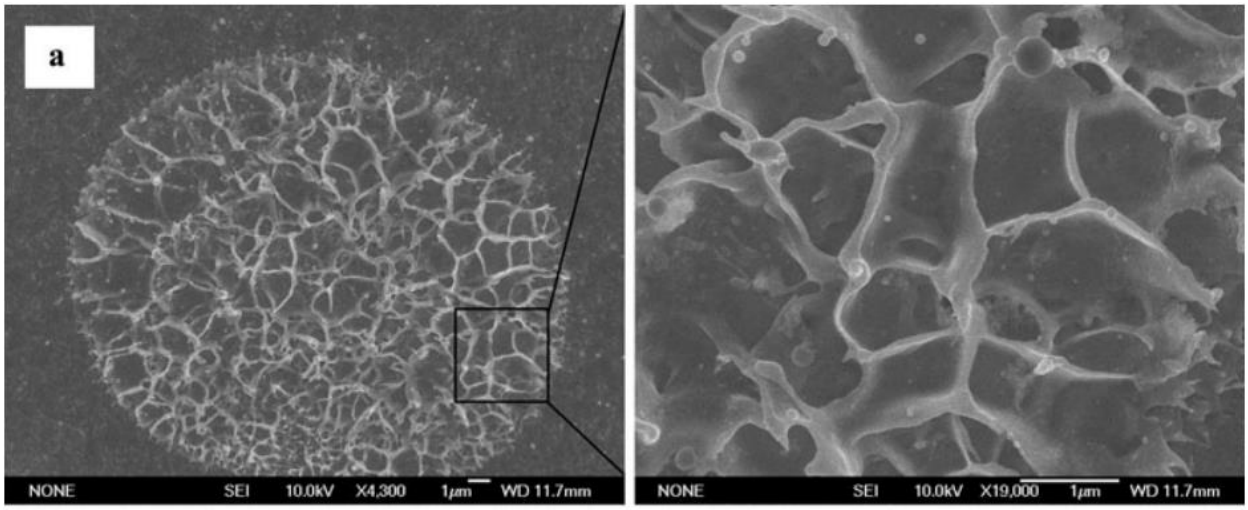

Figure 4.11: Nanostructuring of silver film by femtosecond laser ablation. Adopted from [28]**.**

To cross section these structures a protective layer of platinum was deposited onto the sample. This protective layer prevents ion damage and unwanted milling of small structures on the sample surface. Figure 4.12 includes an SEM image of before and after the milling process. In the before image the deposited platinum can be seen applied to the mound.

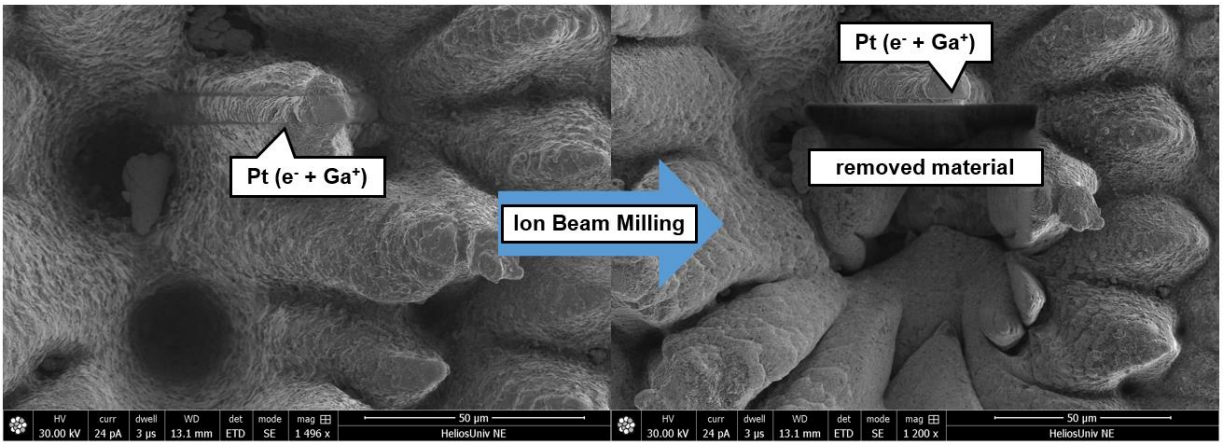

Figure 4.12: Ion beam milling before and after images.

The profile of these surface structures are shown in Fig. 4.14. The purple line represents the approximate grain boundary between original substrate and redeposited materials. The original substrate has large grains and is unmodified by the FLSP process. Above the purple line the material has much smaller grains and is porous with pore diameters ranging from a micron to a few 10s of nanometers.

Material is being removed from the valleys where ablation is occurring at a higher rate and then solidifying. The chaotic nature of fluid mechanics and redeposition creates structure interiors with voids. Figure 4.14 is an image adopted from a paper published covering this research [29]. This image compares an unprocessed silver surface shown in Figure 4.14(a)(c) to the bisected dual-pulse FLSP mound shown in Figure 4.14(b)(d). The smaller grains near the top of Figure 4.14(a) are a result of surface polishing, while within the bulk material the grain sizes are in the range of 5 μm. The mound structures have a mixture of small grains and voids. Moving deeper into the material the grain size becomes larger once the voids are no longer present.

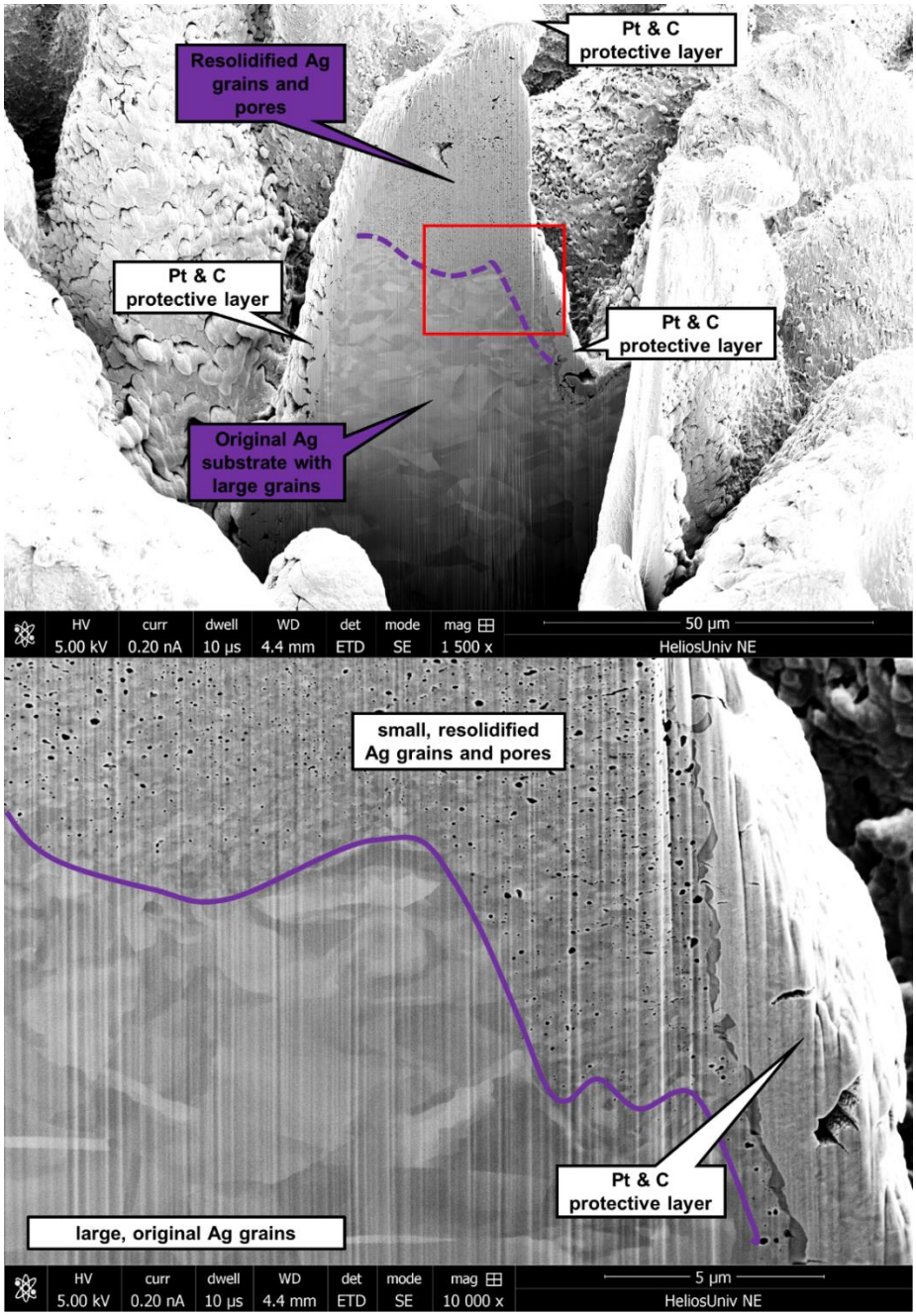

Figure 4.13: Silver structured milled with FIB. The purple line represents the separation between redeposited material and the original substrate.

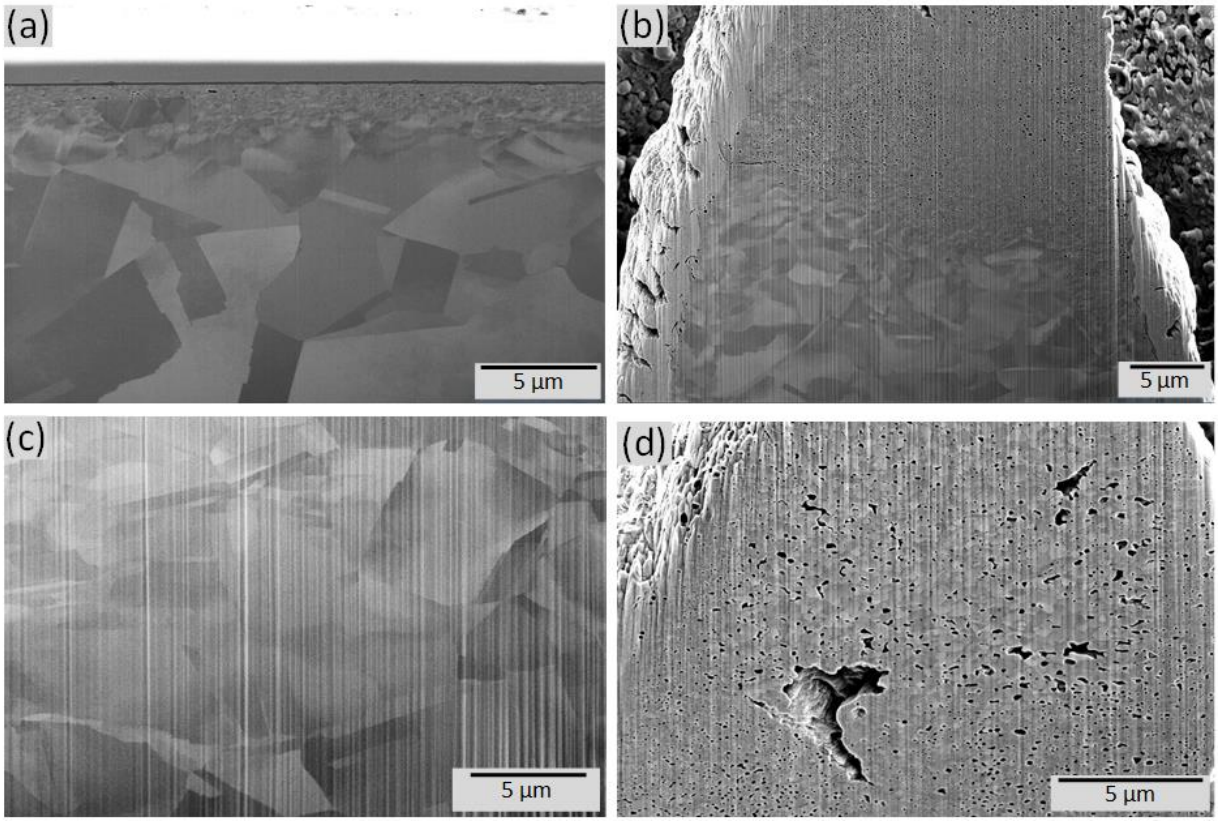

Figure 4.14: SEM images adopted from [29] **which show a) the grain boundary in unprocessed silver b) the grain boundary in dual pulse FLSP structures created in silver c) grain structure within bulk silver d) small and large pores within the silver structures.**

4.4 Dual-pulse structures created through laser rastering

When FLSP is used to functionalize a surface, it will often be applied through laser rastering. This section will cover the bulk functionalization of copper and silver using the laser rastering technique described in Section 2.1. The same laser spot size, pulse energy, pulse width, and fluence were used in this experiment from Table 1. The relationship between pulse separation and bulk structure growth will be investigated.

4.4.1 Silver

Silver surfaces functionalized with dual-pulse FLSP at a rastering velocity of 4 mm/s and a rastering pitch of 30 μm are shown in Figure 4.15. The pulse separation is given in the upper left-hand corner of each SEM image. Using **Error! Reference source not found.** the pulse count for these laser parameters can be calculated. The initial pulse and the delayed pulse will have differing pulse counts because of the differing beam characteristics. The initial and delayed pulses had a spot size of 610 and 520 μm respectively, which result in a pulse count of 3,100 and 2,250 respectively. However, based on the studies of ablation craters, structures only form on the areas covered by both pulses. This would seem to indicate the pulse count using the delayed pulse value of 2,250 would be a better representation of how many laser pulse pairs are involved in structure formation.

For the rastered surfaces structure formation occurs at the same pulse separation as the stationary ablation craters in Figure 4.2. The beginnings of structure formation can be found with an 80 ps separation, however, the most developed structures were created at delay times past 110 ps. As with the stationary ablation craters, for delays extending past 500 ps no structures formed again.

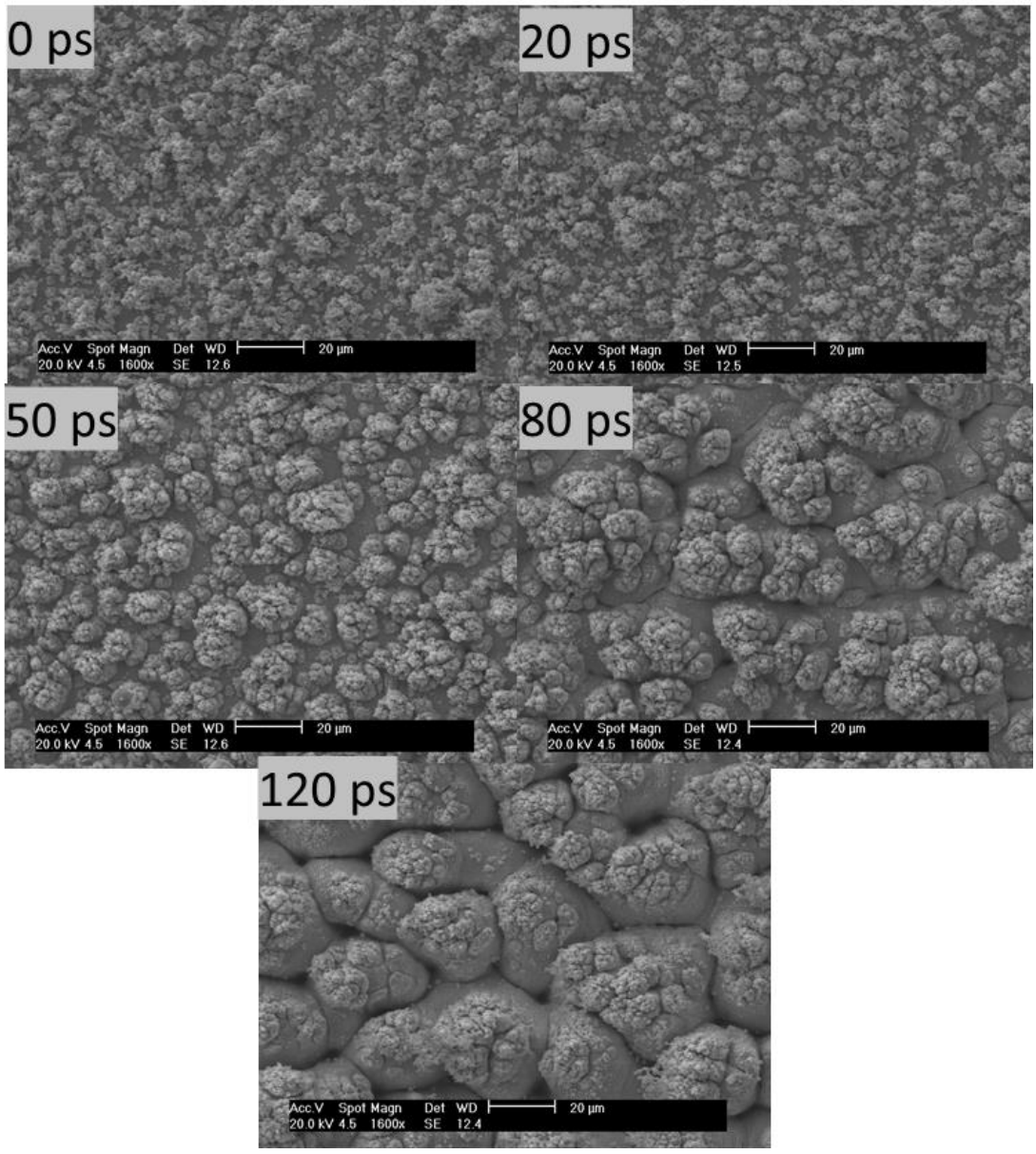

Figure 4.15: SEM images of rastered silver surfaces at 1600x magnification with the delay between the leading and delayed pulse given in picoseconds. The laser fluence used was kept constant from the stationary ablation spots in Figure 4.2 with the rastering velocity being 4 mm/s and 30 micron spacing.

SEM images of single-pulse FLSP compared to dual-pulse FLSP are shown in Fig. 4.17. The single-pulse FLSP rastering (Figure 4.16(b)(c)) was completed with an equal amount of laser pulse energy as the dual-pulse rastering (Figure 4.16(a)), using either pulses from the initial beam path or the delayed beam path shown in Figure 3.1. Both surfaces in Figure 4.16 look much like the surfaces in Figure 4.15 produced using the lower pulse separations.

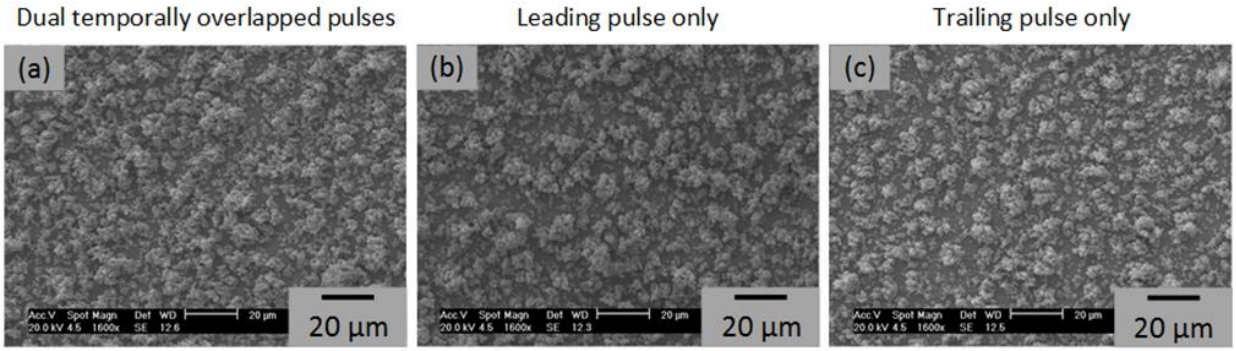

Figure 4.16: SEM images of surfaces after laser rastering with total pulse energy of 4.6 mJ a) dual pulse FLSP with no pulse delay using a peak fluence of 1.55 J/cm^2 and the delayed pulse a peak fluence of 2.17 J/cm^2 b) single pulse FLSP with a peak fluence of 3.08 J/cm^2 c) single pulse FLSP with a peak fluence of 4.32 J/cm^2.

Mound-like surface structures did not form using single-pulse FLSP for any pulse count. A large range of pulse counts and fluences were attempted in finding structures using single-pulse FLSP. Using a spot size of 520 µm, a range of rastering pitches from 75-20 µm, and a range of rastering speeds of 4 mm/s to 0.1 mm/s, which equates to a range of 135,000 to 900 pulse counts. The range of fluences attempted were up to 20 J/cm^2. Only nanoparticulate of varied depth and size was created, no permanent structures formed.

To quantify these surfaces they were measured using the Keyence microscope using a 50X objective. The average structure height is shown in Figure 4.17 along with the standard

deviation. These values were found by measuring the height of 10 mounds chosen randomly. This process was done at 3 different areas on the sample so a total of 30 mounds were measured.

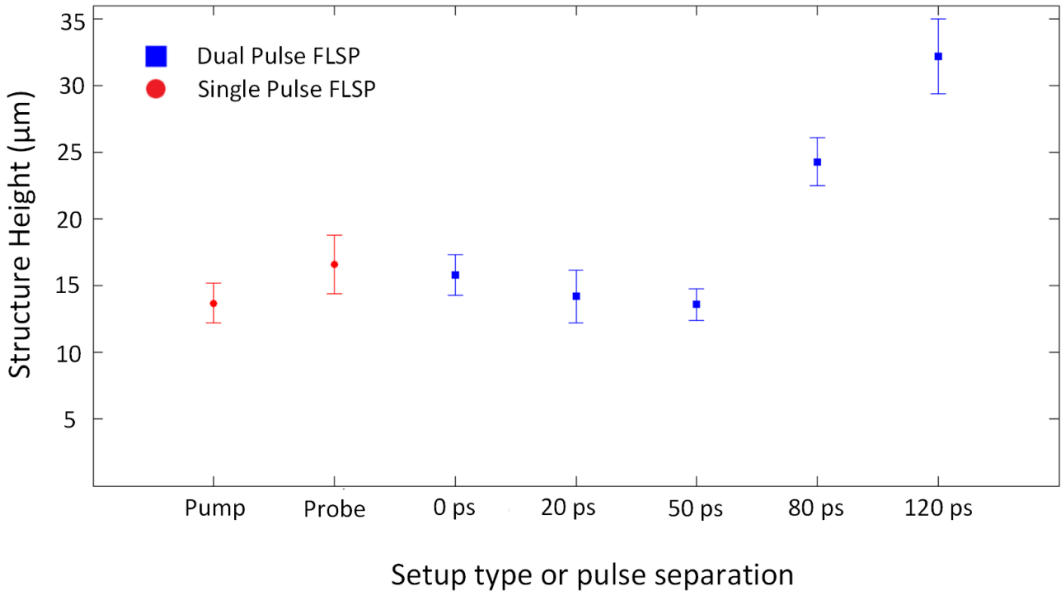

Figure 4.17: Average structure height for silver surfaces functionalized with single or dual pulse FLSP.

The average structure height was approximately the same for the single-pulse FLSP and the dual-pulse FLSP with pulse separations of 0, 20, and 50 ps. Structure size begins to increase at 80 ps and are fully developed at 120 ps. Modifying the fluence and pulse count may result in larger surface structures but nothing larger than 100 µm was produced in this work.

4.4.2 Copper

Dual-pulse rastering was also performed on copper. The same rastering and laser parameters were used from Figure 4.15. The pulse separation between initial pulse and delayed pulse were varied. The results found in Fig. 4.18 match the pulse separation at which structures

form in Figure 4.2. Using a pulse separation of 20 ps resulted in structures with the largest diameter with the fluence and pulse count kept constant.

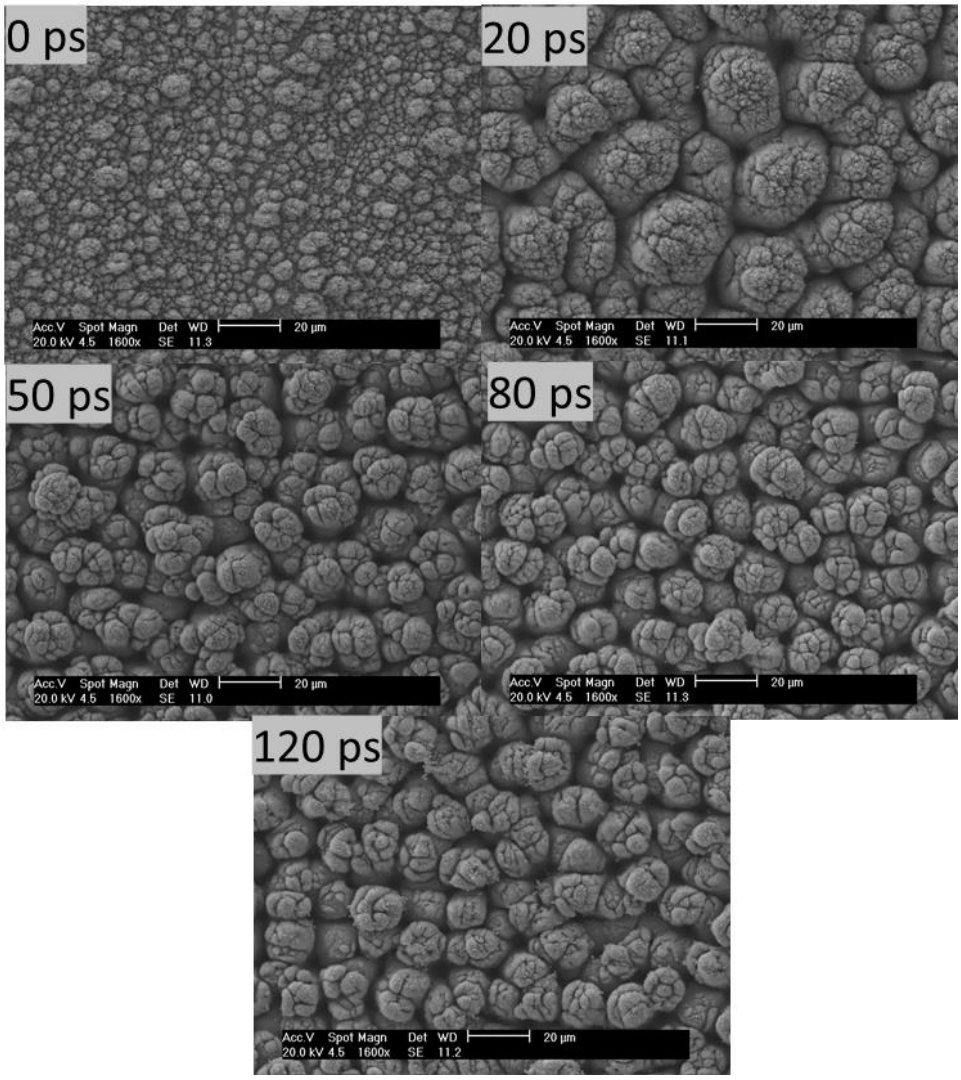

Figure 4.18: SEM images of rastered copper surfaces at 1600x magnification with the delay between the leading and delayed pulse given in picoseconds. The laser fluence used was kept constant from the stationary ablation spots in Figure 4.2 with the rastering velocity being 4 mm/s and 30 micron spacing.

Single-pulse FLSP on copper was somewhat successful at creating surface structures on copper. Two SEM images of surfaces created using single-pulse FLSP with the initial beam at a

peak fluence of 3.08 J/cm^2 and the delay beam at a peak fluence of 4.32 J/cm^2 are shown in Figure 4.19. Surface structures were created with the delay beam because of its higher fluence. While structures were created using single-pulse FLSP they required much more pulse energy to create developed structures when compared to dual-pulse FLSP. Comparing the structures created through dual-pulse FLSP in Figure 4.18 to the structures created through single-pulse FLSP in Figure 4.19 the dual-pulse structures are much more filled in and developed with well defined mounds and valleys.

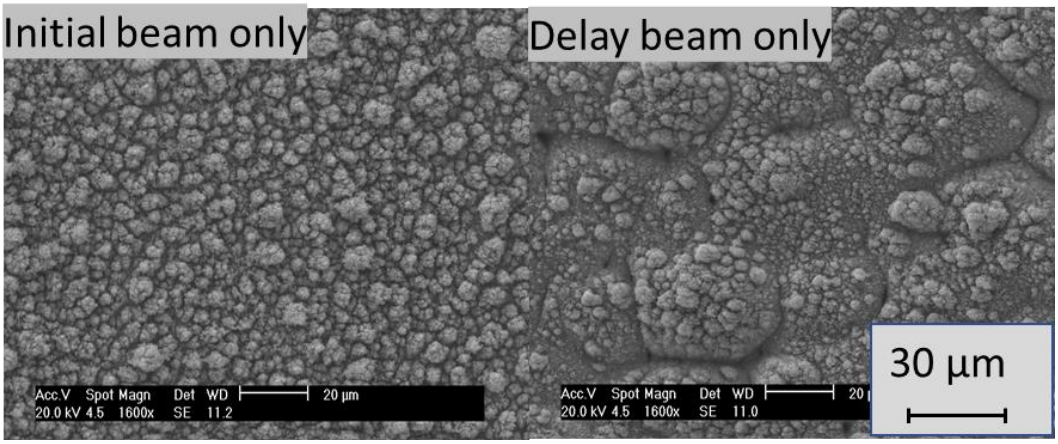

Figure 4.19: SEM images of surfaces after laser rastering with total pulse energy of 4.6 mJ. The same laser parameters were used as in Figure 4.16(b) for the initial beam image and Figure 4.16(c) for the delay beam image.

The LSCM was used to quantify these structures. The same methodology used for the data in Figure 4.17 was used for the data in Figure 4.20. Figure 4.20 shows the average structure height of the structures found in Figure 4.19 (shown in red) and the structures found in Figure 4.18 (shown in blue). Overlapped dual-pulse FLSP and single-pulse FLSP using the initial beam

created a nanoparticulate. The structure height was consistent around 20 μm for dual-pulse FLSP at all values measured above 0 ps.

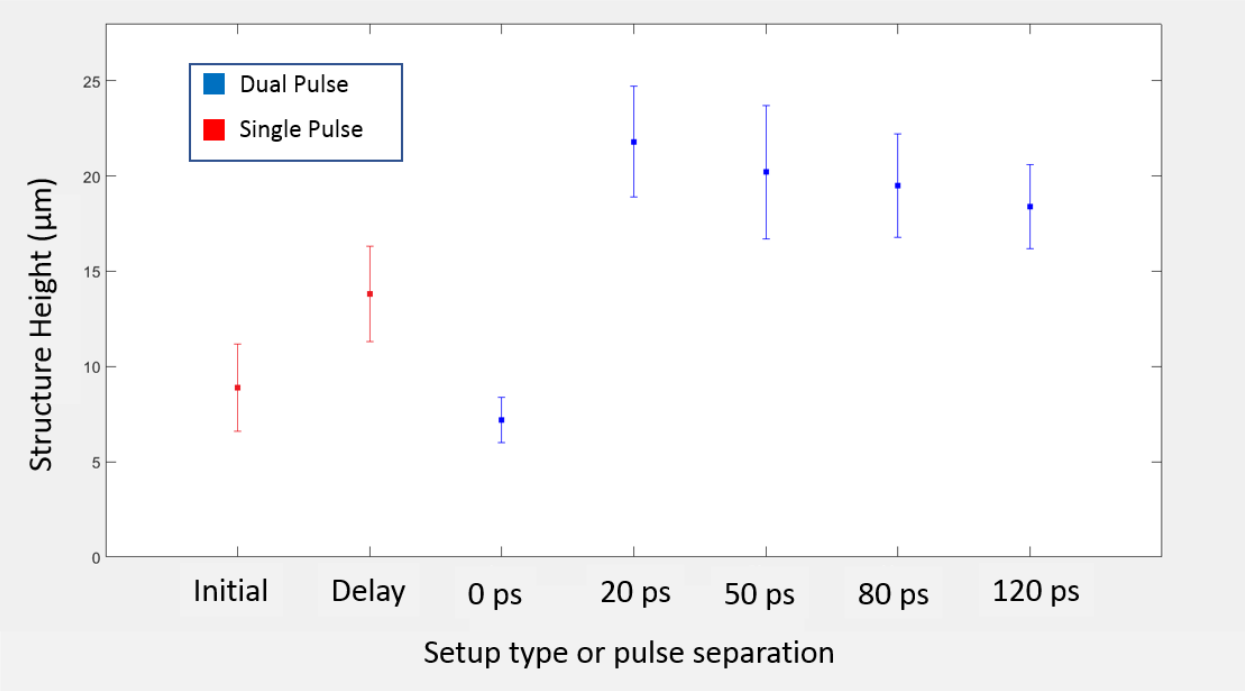

Figure 4.20: Average structure height for copper surfaces functionalized with single or dual pulse FLSP. The data bars give the standard deviation of surface structures.

4.5 Theory explaining dual-pulse FLSP

Ultra-short laser pulses have unique interactions with matter. The materials studied in this thesis have a characteristic relaxation time in the picoseconds. This relaxation time is represented in the electron-phonon transfer time and the electron heat conduction time. For femtosecond laser pulses, material removal occurs due to thermal vaporization at high laser intensities or due to Coulomb explosion at low laser intensities [30]. The FLSP process requires high laser intensities so the primary mechanism of ablation is thermal vaporization.

The process of thermal vaporization creates a surface plasma which is highly reflective and treated like a conductor. The laser is partially reflected and partially absorbed at a skin depth of δ shown in Figure 4.21. The effect of plasma shielding has been studied widely [14], [27]. The absorption of a secondary pulse to reheat a laser plasma is a well-known use of dual-pulse LIBS, which was discussed in the previous chapters.

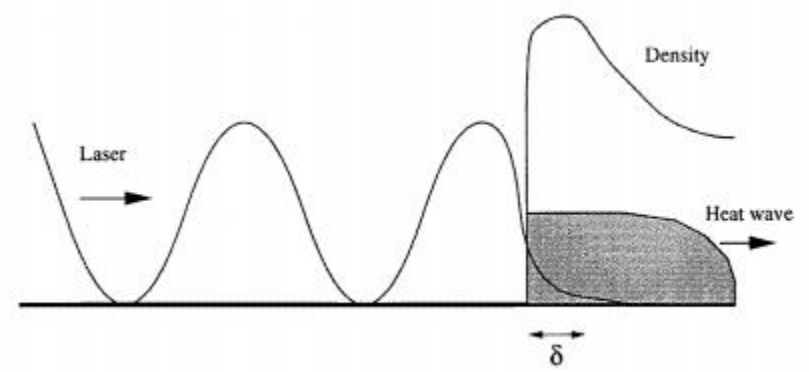

Figure 4.21: Schematic of short pulse heating of solid-density plasma. Adopted from [30]**.**

One possibility for the difference in dynamics for dual-pulse versus single-pulse FLSP is that the laser pulses are being partially reflected by the creation of a laser induced air plasma. A laser pulse will break down air into a plasma if the intensity is sufficient. The plasma created is a mixture of ions and electrons which is highly reflective. The first few femtoseconds of the laser pulse would be creating a plasma and the trailing end of the pulse is being reflected. When the dual-pulse setup is used, more energy is coupled into the material by reducing the fraction of the laser pulse being reflected or absorbed by the plasma.

A diagram of a laser pulse being partially reflected by an air plasma is shown in Fig. 4.23. If the dual-pulse setup is reducing the rate at which the laser pulse is being reflected, then

the laser power measured after focus should be higher with a pulse separation versus overlapped pulses.

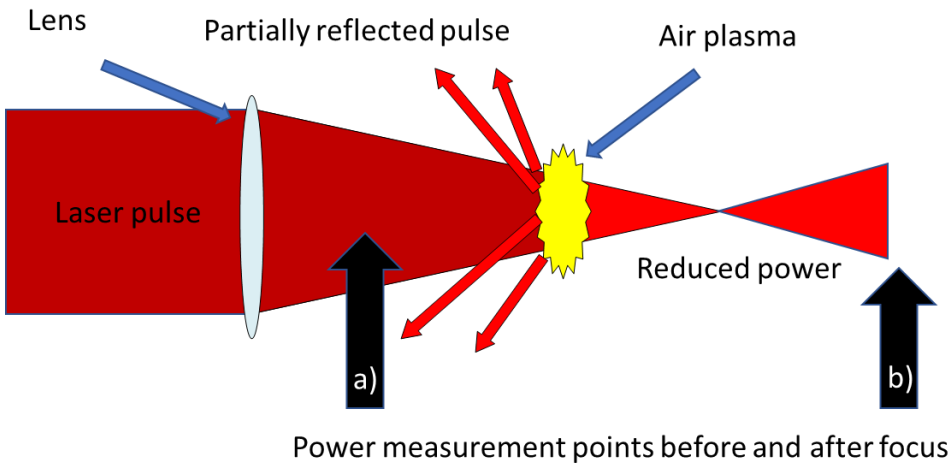

Figure 4.22: Laser pulse partially reflected

In this experiment the power was measured at point (a) and then at point (b) on Figure 4.22. This was completed for laser powers of 250 mW, 1,000 mW, 2,000 mW, and 4,000 mW and at pulse separations of 0 ps, and 133.4 ps. A single pulse train was also tested by routing the laser power through the delayed arm of the experimental setup (yellow path in Figure 3.1) and blocking off the initial beam (orange path in Figure 3.1). An image of this experiment measuring the power at point (b) is shown in Figure 4.23. The air plasma is circled in red and the laser plasma continuum can be seen on the power meter.

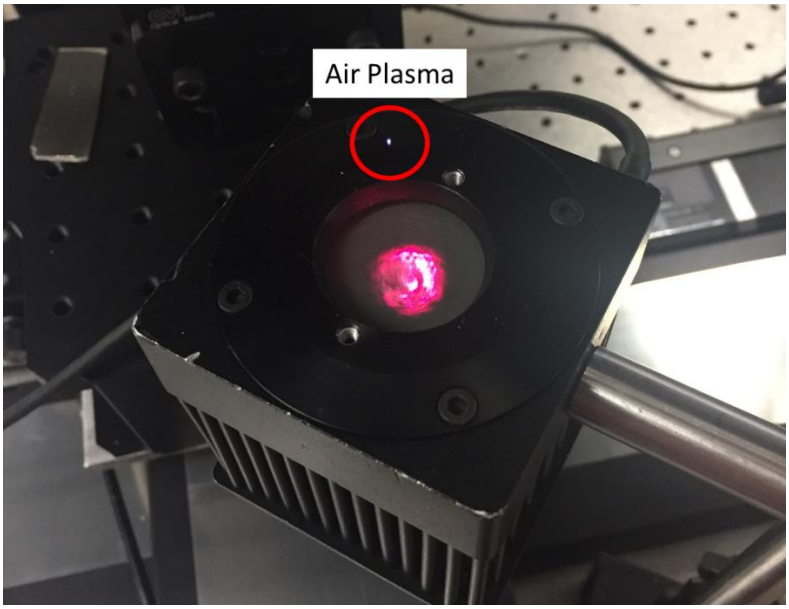

Figure 4.23: Laser power measurement after air plasma.

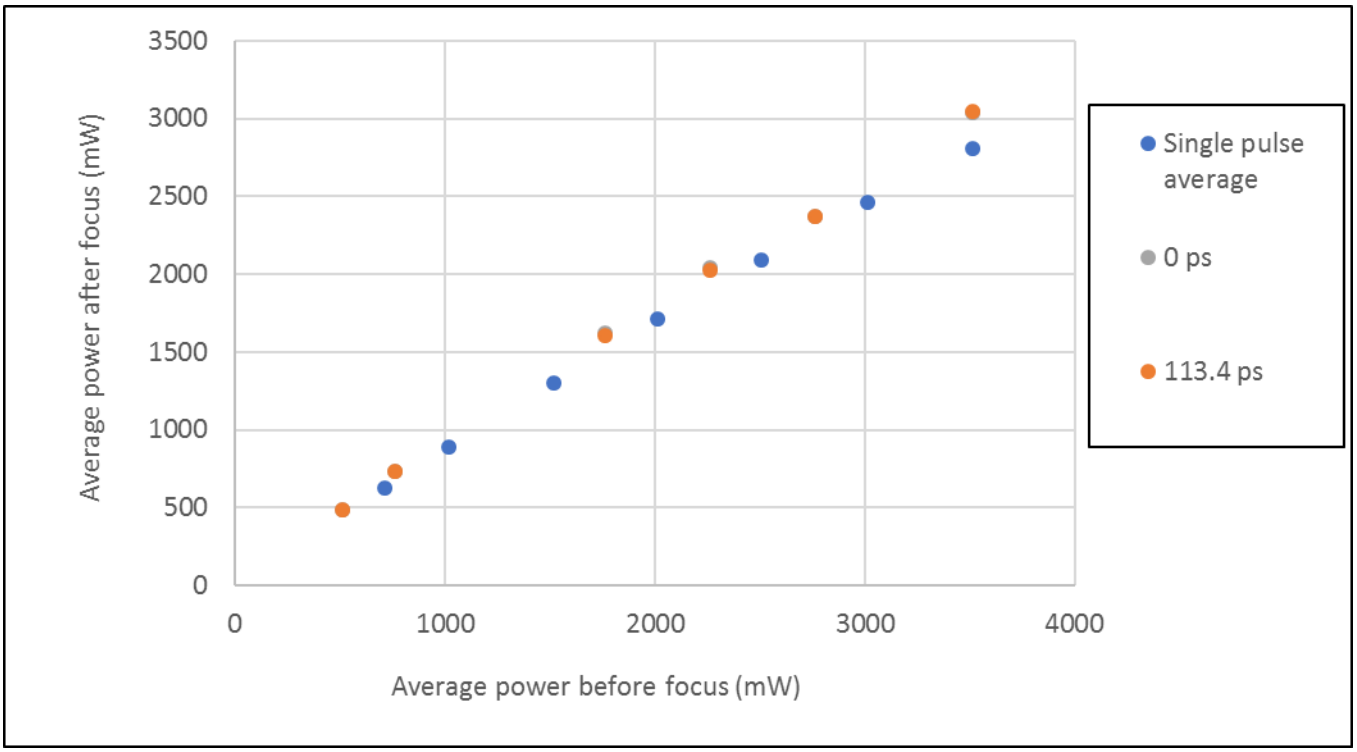

Figure 4.24: Air plasma power loss test for different pulse separations. In reference to Figure 4.22, power measured at point (a) is on the x axis and power measured at point (b) is on the y axis. The power was measured over 5 seconds and the average value was recorded.

A plot of the air plasma power test is given in Fig. 4.24. There appears to be no difference in the amount of power lost traveling through the air plasma when comparing pulse delays of 0 ps and 113.4 ps but there does, however appear to be a marginal difference between the dual-pulse setup at any separation and the single-pulse setup.

It also seems unlikely that this marginal reduction in power lost would account for the dramatic difference in structure formation. The lack of any change in between a pulse separation of 0 ps and a pulse separation of 113.4 ps also points to this being a non-factor in structure formation.

Pump probe research has shown that short pulse laser irradiation can change the optical properties of a material. The reflectivity of silicon [31], and germanium [32] have been shown to decrease in reflectivity after irradiation from a femtosecond laser pulse. Figure 4.25 is adopted from a paper by Bonse et al. using a pump probe setup to study the properties of germanium after femtosecond pulse laser irradiation [32]. Reflectivity does decrease between 40 and 60 percent within the same timeframe as dual-pulse FLSP is effective in copper and silver.

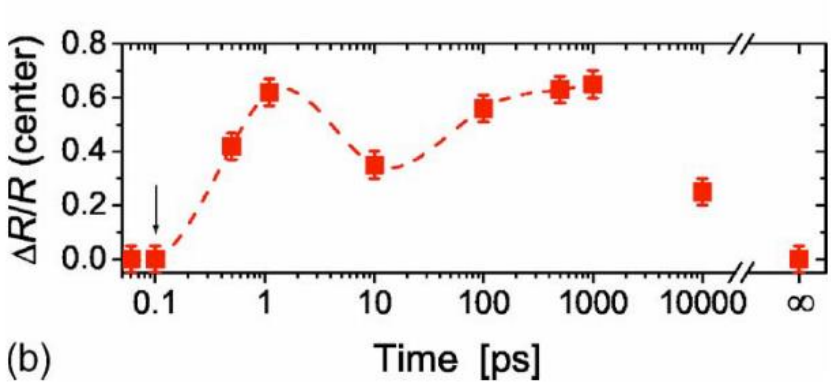

Figure 4.25: Relative reflectivity of germanium after irradiation from a pulse with a peak fluence of 0.83 J/cm^2. Graph adopted from [32]**.**

A similar experiment was performed as to the one done by Bonse et al. using the dual-pulse setup and a high speed InGaAs photodetector with a 175 ps rise time. A polished silver sample was tilted by 20 degrees, so the pulse pair would reflect onto the photodiode. The voltage was measured using a high-speed oscilloscope from Tektronix with an 80 GS/s sampling rate. A diagram of this setup is shown in Figure 4.26. A chopping wheel was used to select single pulse pairs when the shutter was activated. Two pulse separations were tested at 0 ps and 200 ps. The sample was translated after each pulse to avoid damage from the previous ablation crater. Five pulses at each delay time were measured.

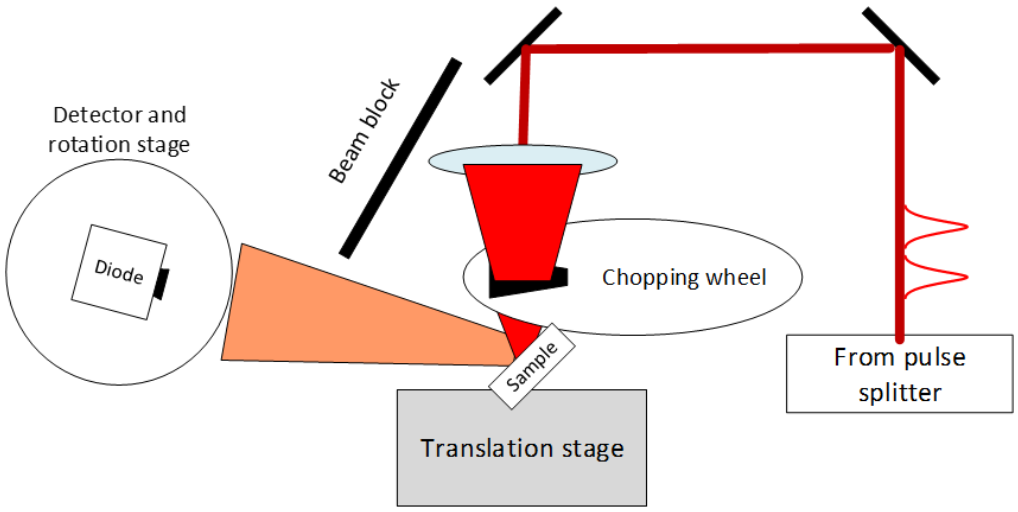

Figure 4.26: Experimental setup for dual pulse reflectivity measurements.

The peak voltage and the integrated voltage over the signal lifetime were measured. The peak voltage is a measurement of peak intensity and the integrated voltage would be a measurement of integrated intensity or energy per area squared. Figure 4.27 shows the average measured values and the standard deviation.

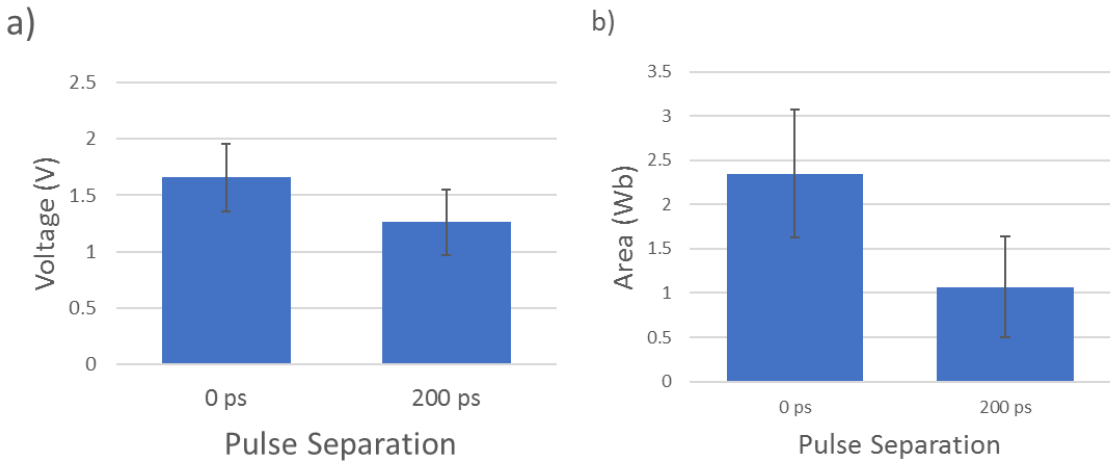

Figure 4.27: Dual-pulse reflective intensity measurements at a) peak voltage (peak intensity) and b) integrated voltage (integrated intensity). Both tests used pulse separations of 0 ps and 200 ps. The bars represent standard deviation.

The photodiode does not respond fast enough to measure the full waveform for each individual pulse when they are this close together so the two signals overlap. It is possible to measure both pulses together and look for a relative difference between overlapped and separated pulse pairs. With pulse pairs which are separated longer than the photodetector rise time of 175 ps we would expect to see an increase in the integrated voltage because the second pulse is reaching the photodetector while the signal of the first pulse is decaying. The opposite is observed as the integrated voltage is lower for the longer delay time. It does appear that the initial pulse is affecting the reflectivity of the sample surface.

Given the thermal dynamic nature of structure formation created with FLSP another theory behind the dynamics of dual-pulse FLSP is an increase in plasma temperature. Dual-pulse LIBS work has shown that the second pulse can reheat a cooling plasma [14], [27].

Laser plasma temperature was measured using an Andor spectrometer and a method outlined in a 2013 paper by Freeman et al. [33]. Using a Bolzmann plot the intensity ratio of spectral lines was calculated using **Error! Reference source not found.**.

$$ln\left(\frac{l_{ki}\lambda}{g_k A_{ki}}\right) = -\frac{1}{k_B T_{ex}} E_j + ln\left(\frac{hen_e}{4\pi U(T_{ex})}\right), \quad (5)$$

The excitation temperature can be determined by the slope of the left hand side of **Error! Reference source not found.** versus the value of E_j or the energy of the upper state. The value I_{ki} is the intensity of transition, λ is the wavelength, A_{ki} is the transition probability, and g_k is the degeneracy of the upper state. These values can be found on the National Institute for Standards and Technology website [34].

Using a pulse separation time of 0 ps and 125 ps the plasma temperature was measured for copper dual-pulse laser ablation. Copper was selected as its spectral lines were easier to detect than silver. The plasma temperature was measured 400 ps after the initial pulse reached the sample to avoid spectrometer saturation at 800 nm from the laser pulse. The sample was sanded and polished. Six trials were conducted for both pulse separation times. The peak fluence used was 2.02 J/cm^2 for the initial pulse and 2.31 J/cm^2 for the delayed pulse. Each ablation crater was created with pulse pair count of 500.

The average calculated temperature with the standard deviation is given in Figure 4.28. The laser induced plasma temperature was 12.2 x 10^3 ± 1.0 x10^3 K for a 0 ps pulse separation and 16.0 x10^3 ± 2.9 x10^3 K for a 125 ps pulse separation.

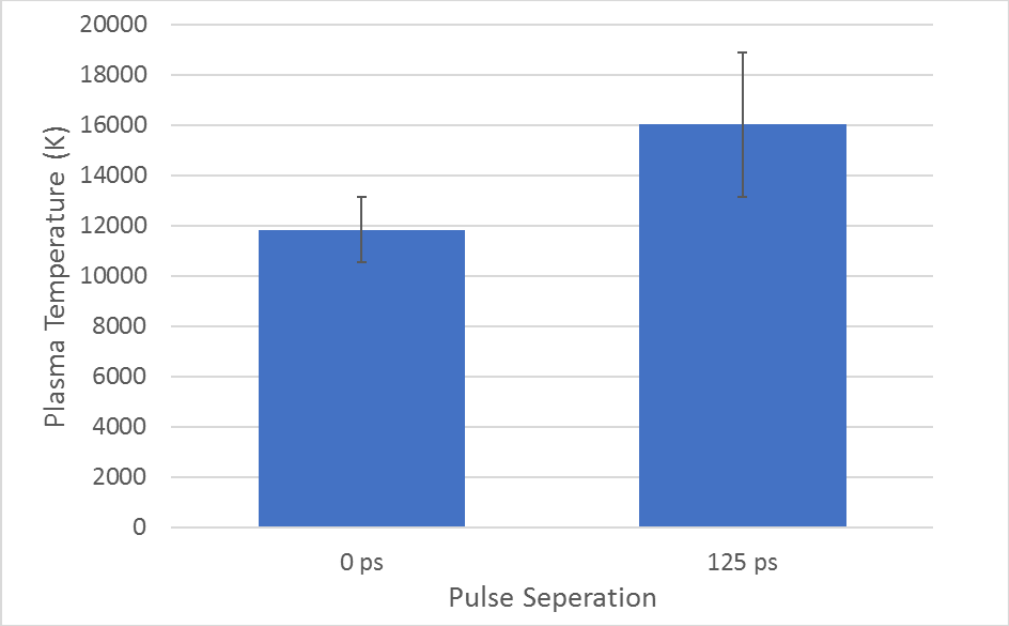

Figure 4.28: Laser induced plasma temperature at pulse separation times of 0 ps and 125 ps.

This increase in plasma temperature was expected. Past work completed on dual-pulse LIBS has shown double pulse plasmas are 1,000-1,500 K higher than the temperatures created by a

single pulse [35]. The increase in average plasma temperature for this experiment was 3,800 K between the two pulse separations. This difference between plasma temperature increase in the literature and the plasma temperature increase in the experiments in this thesis may be due to the higher overall pulse energy used for dual pulse FLSP. The calculated plasma temperature for 0 ps pulses also matches plasma temperature measurements for copper using single-pulse ablation [33]. Further research is needed into the part that laser induced plasma plays in FLSP.

Chapter 5: Conclusion

Mound like micro/nanostructures were created on silver and copper using dual pulse femtosecond laser surface processing (FLSP). The influence of pulse separation was investigated and a pulse separation of approximately 100 ps is needed to induce structure formation. Stationary ablation spots and rastered surface areas were both studied and found to create surface structures. The structures created within the stationary ablation craters were found to be similar in composition to past structures created on other materials using the single-pulse FLSP method.

Dual-pulse FLSP couples more energy into the sample. The initial pulse changes the material optical characteristics and causes it to be more absorbing and less reflective. It is possible this is a large component of what makes dual-pulse FLSP effective.

References

[1] C. A. Zuhlke, T. P. Anderson, and D. R. Alexander, "Formation of multiscale surface structures on nickel via above surface growth and below surface growth mechanisms using femtosecond laser pulses," *Opt. Express*, vol. 21, no. 7, p. 8460, 2013.

[2] A. Y. Vorobyev and C. Guo, "Direct femtosecond laser surface nano/microstructuring and its applications," *Laser Photon. Rev.*, vol. 7, no. 3, pp. 385–407, May 2013.

[3] C. Kruse *et al.*, "Extraordinary Shifts of the Leidenfrost Temperature from Multiscale Micro/Nanostructured Surfaces," 2013.

[4] C. M. Kruse, "Heat Transfer Enhancement and Applications of Femtosecond Laser Processed Metallic Surfaces: magistrska naloga," pp. 1–100, 2014.

[5] C. Kruse *et al.*, "Self-propelled droplets on heated surfaces with angled self-assembled micro/nanostructures," *Microfluid. Nanofluidics*, vol. 18, no. 5–6, pp. 1417–1424, 2015.

[6] a. Y. Vorobyev and C. Guo, "Femtosecond laser structuring of titanium implants," *Appl. Surf. Sci.*, vol. 253, no. 17, pp. 7272–7280, Jun. 2007.

[7] C. A. Zuhlke *et al.*, "Superhydrophobic metallic surfaces functionalized via femtosecond laser surface processing for long term air film retention when submerged in liquid," vol. 9351, p. 93510J, 2015.

[8] S. Link, C. Burda, B. Nikoobakht, and M. A. El-Sayed, "Laser-Induced Shape Changes of Colloidal Gold Nanorods Using Femtosecond and Nanosecond Laser Pulses," *J. Phys. Chem. B*, vol. 104, no. 26, pp. 6152–6163, 2000.

[9] A. A. Ionin *et al.*, “Femtosecond laser color marking of metal and semiconductor surfaces,” *Appl. Phys. A Mater. Sci. Process.*, vol. 107, no. 2, pp. 301–305, 2012.

[10] W. Gao *et al.*, “Direct laser writing of micro-supercapacitors on hydrated graphite oxide films,” *Nat. Nanotechnol.*, vol. 6, no. 8, pp. 496–500, 2011.

[11] D. N. Stratis, K. L. Eland, and S. M. Angel, “Dual-pulse LIBS using a pre-ablation spark for enhanced ablation and emission,” *Appl. Spectrosc.*, vol. 54, no. 9, pp. 1270–1274, 2000.

[12] R. S. Adrain, J. Watson, M. A. Khater, P. Van Kampen, and J. T. Costello, “Laser-induced breakdown spectroscopy of steel samples using multiple Q-switch Nd:YAG laser pulses,” 1995.

[13] F. Colao, V. Lazic, R. Fantoni, and S. Pershin, “A comparison of single and double pulse laser-induced breakdown spectroscopy of aluminum samples,” *Spectrochim. Acta Part B At. Spectrosc.*, vol. 57, no. 7, pp. 1167–1179, 2002.

[14] V. I. Babushok, F. C. DeLucia, J. L. Gottfried, C. A. Munson, and A. W. Miziolek, “Double pulse laser ablation and plasma: Laser induced breakdown spectroscopy signal enhancement,” *Spectrochim. Acta - Part B At. Spectrosc.*, vol. 61, no. 9, pp. 999–1014, 2006.

[15] J. Bonse, J. M. Wrobel, K. W. Brzezinka, N. Esser, and W. Kautek, “Femtosecond laser irradiation of indium phosphide in air: Raman spectroscopic and atomic force microscopic investigations,” *Appl. Surf. Sci.*, vol. 202, no. 3–4, pp. 272–282, 2002.

[16] R. R. Brooks, *Noble Metals and Biological Systems: Their Role in Medicine, Mineral*

Exploration, and the Environment. CRC Press, 1992.

[17] C. A. Zuhlke, J. Bruce, T. P. Anderson, D. R. Alexander, and C. G. Parigger, "A fundamental understanding of the dependence of the laser-induced breakdown spectroscopy (LIBS) signal strength on the complex focusing dynamics of femtosecond laser pulses on either side of the focus," *Appl. Spectrosc.*, vol. 68, no. 9, pp. 1021–1029, 2015.

[18] C. A. Zuhlke, "Control and understanding of the formation of micro/nanostructured metal surfaces using femtosecond laser pulses," *ProQuest*, 2012.

[19] E. Peng, "Understanding the formation of micro/nanoscale structures on metal surfaces by ultrafast pulse laser processing," 2017.

[20] H. Fujiwara, "Spectroscopic ellipsometry : principles and applications / Hiroyuki Fujiwara." John Wiley & Sons, Hoboken, NJ :, p. 0-0 SE-.

[21] G. Paul, *Short Pulse Laser Interaction with Matter*. Imperial College Press, 2005.

[22] E. D. Potter, J. L. Herek, S. Pedersen, Q. Liu, and A. H. Zewail, "Femtosecond laser control of a chemical reaction," *Nature*, vol. 355, p. 66, Jan. 1992.

[23] C. K. Wilson, "Application of Femtosecond Laser Surface Processed Electrodes in Electrolysis of Water," 2014.

[24] U. of N.- Lincoln, "Nano-Engineering Research Core Facility." [Online]. Available: https://engineering.unl.edu/nercf/fei-helios-fibsem-650/.

[25] N. L. Lahaye, S. S. Harilal, P. K. Diwakar, and A. Hassanein, "The effect of laser pulse duration on ICP-MS signal intensity, elemental fractionation, and detection limits in fs-

LA-ICP-MS," *J. Anal. At. Spectrom.*, vol. 28, no. 11, pp. 1781–1787, 2013.

[26] A. I. Kuznetsov, J. Koch, and B. N. Chichkov, "Nanostructuring of thin gold films by femtosecond lasers," *Appl. Phys. A Mater. Sci. Process.*, vol. 94, no. 2, pp. 221–230, 2009.

[27] A. Semerok and C. Dutouquet, "Ultrashort double pulse laser ablation of metals," *Thin Solid Films*, vol. 453–454, pp. 501–505, 2004.

[28] Y. Dai, M. He, H. Bian, B. Lu, X. Yan, and G. Ma, "Femtosecond laser nanostructuring of silver film," *Appl. Phys. A Mater. Sci. Process.*, vol. 106, no. 3, pp. 567–574, 2012.

[29] N. Roth, C. Zuhlke, E. Peng, S. Hansen, J. E. Shield, and D. Alexander, "Creation of micro/nano surface structures on silver using collinear double femtosecond laser pulses with different pulse separation," *Multiscale Multidiscip. Model. Exp. Des.*, Apr. 2018.

[30] S. Harilal, *Femtosecond laser ablation: Fundamentals and Applications in "Laser Induced Breakdown Spectroscopy: Theory and Applications."* 2014.

[31] T. Y. Choi, D. J. Hwang, and C. P. Grigoropoulos, "Femtosecond laser induced ablation of crystalline silicon upon double beam irradiation," *Appl. Surf. Sci.*, vol. 197–198, pp. 720–725, 2002.

[32] J. Bonse, G. Bachelier, J. Siegel, and J. Solis, "Time- and space-resolved dynamics of melting, ablation, and solidification phenomena induced by femtosecond laser pulses in germanium," *Phys. Rev. B - Condens. Matter Mater. Phys.*, vol. 74, no. 13, pp. 1–13, 2006.

[33] J. R. Freeman, S. S. Harilal, P. K. Diwakar, B. Verhoff, and A. Hassanein, "Comparison

of optical emission from nanosecond and femtosecond laser produced plasma in atmosphere and vacuum conditions," *Spectrochim. Acta - Part B At. Spectrosc.*, vol. 87, pp. 43–50, 2013.

[34] "Atomic Spectra - Physical Measurment Laboratory." [Online]. Available: https://physics.nist.gov/PhysRefData/ASD/lines_form.html.

[35] R. Sattmann and R. Noll, "Laser-induced breakdown spectroscopy of steel samples using multiple Q-switch Nd:YAG laser pulses," *J. Phys. D. Appl. Phys.*, vol. 2181, pp. 2181–2187, 1995.